Are soil-freezing characteristic curves important for cryohydrogeologic model results?

Audrey Woo
Department of Earth and Planetary Sciences
McGill University, Montreal

April 2022

A thesis submitted to McGill University in partial fulfilment of the requirements of the degree of
Master of Science

Table of Contents

List of Figures

List of Tables

Abstract

In cold regions, the unfrozen water content plays an important role in a number of processes, including permafrost thaw, groundwater-surface water exchange, and heat and solute transport in soils. The relationship between unfrozen water content and sub-freezing temperatures (or suction at the ice-water interface) is known as the soil-freezing characteristic curve (SFCC). Previous studies have shown that considering the unfrozen water content can significantly improve accuracy in heat and water transport modelling. However, the differences in how various soil-freezing functions and parameterizations affect hydrogeologic properties and thermal regimes are not well understood. In this thesis, SUTRA-ice, a numerical model that couples groundwater flow and energy transport with dynamic freeze-thaw processes, is used to simulate and compare the performance and parameterization of three widely used SFCC functions (exponential, piecewise linear, and power law). The shape of the SFCC is dependent on parameters including the residual unfrozen water content, freezing point depression, or empirical constants characteristic of a given soil. A two-dimensional homogeneous model with time-dependent thermal and hydrological surface boundary conditions represents a simple permafrost cross-section. Results show that the type and parameterization of the SFCC significantly affects permafrost evolution, active zone dynamics, and stream discharge in coupled heat and water transfer modelling of frozen soil. Depending on the SFCC used, the residual liquid water saturation and freezing point depression can control the level of ice saturation in the model, talik and permafrost formation, as well as the thickness of the active layer.

Résumé

Dans les régions froides, la teneur en eau non gelée joue un rôle important dans un certain nombre de processus, notamment le dégel du pergélisol, les échanges entre les eaux souterraines et les eaux de surface et le transport de la chaleur et des solutés. La relation entre la teneur en eau non gelée et les températures inférieures au point de congélation (ou succion à l'interface glace-eau) est connue sous le nom de soil-freezing characteristic curve (SFCC). Des études antérieures ont montré que la prise en compte de la teneur en eau non gelée peut améliorer considérablement la précision de la modélisation du transport de la chaleur et de l'eau. Cependant, les différences dans la façon dont diverses fonctions et paramétrisations de gel du sol affectent les propriétés hydrogéologiques et les régimes thermiques ne sont pas bien comprises. Dans cette thèse, SUTRA-ice, un modèle numérique qui couple l'écoulement des eaux souterraines et le transport d'énergie avec des processus dynamiques de gel-dégel, est utilisé pour simuler et comparer les performances et la paramétrisation de trois fonctions SFCC largement utilisées (exponentielle, linéaire par morceaux et loi de puissance). La forme du SFCC dépend de paramètres tels que la teneur résiduelle en eau non gelée, l'intervalle des températures de gel ou les constantes empiriques caractéristiques d'un sol donné. Un modèle homogène à deux dimensions avec des conditions aux limites thermiques et hydrologiques de surface dépendant du temps représente un transect de pergélisol. Les résultats montrent que le type et la paramétrisation du SFCC affectent de manière significative l'évolution du pergélisol, la dynamique de la zone active et le débit des cours d'eau dans la modélisation couplée du transfert de chaleur et d'eau du sol gelé. Selon le SFCC utilisé, la saturation en eau liquide résiduelle et l'intervalle des températures de congélation peuvent contrôler le niveau de saturation en glace dans le modèle, la formation de talik et de pergélisol, ainsi que l'épaisseur de la couche active.

Acknowledgements

First and foremost, I would like to express my deepest gratitude towards my supervisors, Jeffrey McKenzie and Élise Devoie, for their guidance and unwavering support. Not only do I appreciate their patience and expertise, but I am also grateful to have such kind and passionate mentors as role models and friends. Your enthusiasm for science, approachability, and positive attitudes made my MSc experience so interesting and rewarding, and I feel truly lucky to have worked with two incredible scientists that helped me grow as a researcher and as a person. A very special thanks to Pierrick Lamontagne, whose insightful feedback, modelling expertise, and sense of humour made this degree possible. You were always there to discuss and help me with the many questions I had. Thank you for your invaluable advice and the many hours spent talking about science and life.

I would like to thank all the past and present members of the 'Laboratory of Advanced Hydrogeological Modelling and Stuff' notably Laura Lyon, Rob Wu, Lauren Somers, Greg Langston, Emilienne Hamel, Selsey Stribling and Niklas Petersen for their friendship, advice, and motivation. I also wish to thank the EPS administrative team, Anne Kosowski, Kristy Thornton and Angela Di Ninno, for helping me and keeping me on track. I can't forget to acknowledge and thank my 'emotional support team', Fred and George, for the daily dose of serotonin.

Finally, I would like to dedicate this work to my family and friends who have been by my side during this journey. To my friends, who lent an ear and cheered me on when I needed it. To my parents and brothers, for their optimism and constant encouragement. To Raymond, for your unconditional support - from the very beginning to the very end.

1. Introduction

Groundwater is an essential component of Arctic and Subarctic ecosystems. Increasing temperatures and rapid permafrost thaw due to climate change have led to significant changes in Northern hydrological systems (Romanovsky *et al*., 2010; Serreze *et al*., 2000; Walvoord & Kurylyk, 2016). Permafrost degradation has important implications for groundwater-surface water connectivity, spatial and temporal distribution of water, and heat and solute transport processes (Connon *et al*., 2014; Lamontagne-Hallé *et al*., 2018; Romanovsky & Osterkamp, 2000). Thawing permafrost also acts as a positive feedback mechanism as the thickness of the seasonally thawed layer (*i.e.*, active layer) and year-round thawed zones (*i.e.*, taliks) increase, leading to more groundwater flow, subsidence, and further thaw (Walvoord & Kurylyk, 2016). To study the mechanisms associated with permafrost thaw, recent studies have employed predictive models to simulate hydrogeologic and thermal transport of idealized permafrost environments (e.g., Bense *et al*., 2012; Ge *et al*., 2011; McKenzie *et al*., 2007; McKenzie & Voss, 2013).

In cold regions, the amount of unfrozen water is a key parameter for soil thermal and physical properties, and changing this parameter can affect liquid water transport during freezing and thawing processes (Kozlowski, 2004; Wang *et al*., 2017). Due to capillarity and the surface potential energy of soil particles, not all liquid water in frozen soil transforms into ice. This unfrozen water decreases with decreasing temperature and coexists with pore ice (Anderson & Tice, 1972). Solute concentration, particle size distribution, and the chemical and mineralogical nature of the soil matrix influence the unfrozen water content (Chai *et al*., 2018; Jin *et al*., 2020; Qiu *et al*., 2020). The difference in thermal conductivity between liquid water and ice is a key parameter in cold regions engineering (Li *et al*., 2019), due to its influence on the sensitivity of permafrost to energy exchange. Phase change and associated latent heat release are also important controls on the strength of frozen soil (Li *et al*., 2019). Frozen ice-rich soils are characterized by a relatively high bearing capacity and low compressibility compared to the thawed state. Additionally, latent heat is responsible for approximately two orders of magnitude more energy storage in the system, so accurately knowing the ice content is essential to understanding the energetic state of permafrost. Therefore, understanding the behaviour and processes associated with unfrozen water content is essential for engineering applications and climate change research on Arctic hydrogeology.

The soil-freezing characteristic curve (SFCC) describes the relationship between unfrozen water content and sub-zero temperature (Kurylyk & Watanabe, 2013). There have been many different equations and relationships proposed for SFCC. One common approach is to use the similarity between SFCC and soil-water characteristic curve (SWCC), which relates the soil water content to suction at the air-water interface in unfrozen unsaturated soil (e.g., Kozlowski, 2003; Wang *et al*., 2017). Empirical approaches focus on the direct measurement of SFCC using laboratory or *in situ* methods such as dilatometry, time domain reflectometry (TDR), or nuclear magnetic resonance (NMR) (e.g., Ren & Vanapalli, 2019; Yoshikawa & Overduin, 2005). SFCCs can be used as a tool for estimating the resilient modulus of frozen soils, shear strength, and the segregation potential for frost heave (Ren & Vanapalli, 2019). There are currently no studies that focus on choosing the appropriate SFCC parameterization to accurately simulate dynamic freeze-thaw processes in numerical models. The research objective of this thesis is to determine how soil-freezing characteristic curves affect cryohydrogeologic model outcomes such as permafrost formation and hydrologic connectivity. Three different SFCC's (piecewise linear, exponential, and power law) and a range of parameterizations were compared using a two-dimensional coupled groundwater flow and energy transport model.

2. Literature Review

2.1 Cold regions hydrogeology

Approximately 25% of terrestrial land surface in the Northern Hemisphere and 17% of the Earth's exposed land surface is underlain or partially underlain by permafrost – ground that remains at or below 0°C for at least two consecutive years (Gruber, 2012; Romanovsky *et al*., 2002). Arctic temperatures are rising at more than twice the global average rate (Ballinger *et al*., 2020), leading to rapid permafrost thaw and decreased seasonal ground ice (Pepin *et al*., 2015). Frozen ground often acts as an impermeable barrier to groundwater flow (Williams & Smith, 1989). When pore ice melts, the ground permeability increases, which can change patterns of groundwater flow and increase infiltration at the ground surface (McKenzie & Voss, 2013). The flow and discharge of groundwater to surface water bodies occurs primarily in this region above the permafrost table (*i.e.*, supra-permafrost zone) in the seasonally-thawed active layer, or through perennially unfrozen zones called taliks (Walvoord & Kurylyk, 2016).

The seasonal freezing and thawing of the active layer promotes shallow supra-permafrost groundwater flow early in the thaw season and allows for deeper groundwater flow as the thawing front moves progressively downward in the summer (Kurylyk & Walvoord, 2021). Active layer thickness typically ranges from tens of centimetres to a few metres depending on climatic conditions, landscape factors affecting the surface energy balance, and soil physical and thermal properties. If the frozen soil beneath the thawing front is ice-saturated (thus relatively impermeable), the active layer can function as a shallow perched aquifer that controls runoff and streamflow response to snowmelt and precipitation, as well as solute transport and biogeochemical cycling (Walvoord & Kurylyk, 2016). Increases in baseflow in headwater catchments have been attributed to active layer thickening (Sjöberg *et al*., 2016), especially in regions dominated by supra-permafrost flow.

2.2 Modelling soil freezing processes

Numerical modelling is a useful tool to study how hydrologic systems function and change over time. Numerical groundwater models for cold regions, or cryohydrogeologic models, must represent both energy transport and water flow and therefore require solving fully coupled partial differential equations describing heat transport and unsaturated flow (Grenier *et al*., 2018). The accurate representation of permafrost and seasonal freeze/thaw in multi-year cryohydrogeological models is essential because the presence of frozen soil influences not only the hydrology, but also the thermodynamics, soil chemistry, structural stability, and ecology of regions experiencing freezing soils (Devoie, 2020).

Most groundwater models are based on a multidimensional form of Darcy's Law and use an energy transport equation to describe heat transfer through conduction, advection, and latent heat release and absorption. The modified version of the USGS Saturated-Unsaturated Transport Model (SUTRA-ice) can be used in cryohydrogeological heuristic studies ranging from small field sites to large scale aquifers (McKenzie *et al*., 2007; Voss & Provost, 2010). Energy transport in SUTRA-ice is governed by:

$$C_{eff}\frac{\partial T}{\partial t} = -\varepsilon S_L \rho_L c_L \underline{v} \cdot \underline{\nabla} T + \underline{\nabla} \cdot \left(\underline{\underline{\lambda_{eff}}} \underline{\nabla} T \right) + Q_P c_L (T^* - T) + \varepsilon S_L \rho_L \gamma_L + (1-\varepsilon)\rho_S \gamma_S \tag{1}$$

where C_{eff} is the effective bulk heat capacity of the matrix ($E\cdot L^{-3}\cdot{}^{\circ}C^{-1}$; Equation 2), c_L is the specific heat of liquid water ($E\cdot M^{-1}\cdot{}^{\circ}C^{-1}$), $\underline{v}$ is the average groundwater velocity vector ($L\cdot t^{-1}$), $\underline{\underline{\lambda_{eff}}}$ is the effective thermal conductivity tensor of the matrix ($E\cdot t^{-1}\cdot L^{-1}\cdot{}^{\circ}C^{-1}$), T^* is the temperature of the fluid (°C), ρ_S is the solid grains density ($M\cdot L^{-3}$), and γ_L and γ_S are distributed energy sources or sinks respectively ($E\cdot M^{-1}\cdot t^{-1}$). See Table 1 for a full list of parameters.

When the simulated air temperature drops below the freezing point of the soil, a freezing front (0°C isotherm) moves into the subsurface as a function of the imbalance associated with the heat supplied versus the heat transferred elsewhere in the model domain (Ren *et al*., 2017). As the freezing front advances, the upper portion of the soil becomes frozen while the lower portion remains unfrozen, with a partially frozen layer existing between the frozen and unfrozen soil layers.

The most common benchmark for testing and validating cryohydrogeologic models is the Lunardini analytical solution (1988) that solves for an advancing freezing front into a semi-infinite domain through time. The solution divides the freezing interval in a semi-infinite domain into three zones: unfrozen, partially frozen (or "mushy"), and fully frozen (Figure 1). The use of freezing front models (e.g., Devoie & Craig, 2020) to benchmark and validate numerical codes is a common approach. The SUTRA-ice code successfully replicated the Lunardini solution and the InterFrost benchmark problems (Grenier *et al*., 2018; McKenzie *et al*., 2007; Rühaak *et al*., 2015).

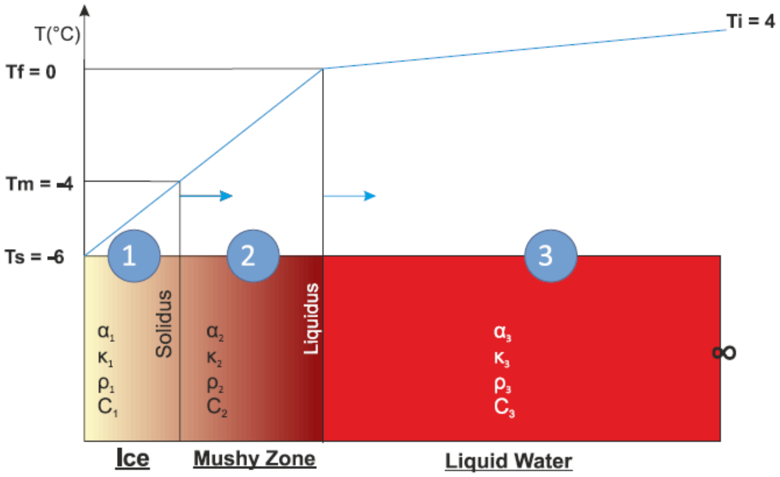

Figure 1. Graphical representation of the Lunardini analytical solution for a propagating freezing front with three zones (i.e., ice, mushy, and liquid water). Here freezing occurs between -4 and 0°C. (Figure from Rühaak *et al*., 2015).

Models of subsurface heat transport in cold regions must incorporate changes in thermal and hydraulic properties as a function of ice content. SUTRA-ice simulates the phase transformation of porewater to ice over a range of sub-freezing temperatures, as well as the associated changes in heat capacity, thermal conductivity, relative permeability, density, and latent heat of formation (McKenzie *et al*., 2007). The effective heat capacity in SUTRA-ice is calculated with a weighted arithmetic average of the heat capacities of the matrix constituents (*i.e.*, liquid water, ice, and solid grains) and includes the release or absorption of energy due to latent heat during the liquid and solid water phase changes:

$$C_{eff} = \varepsilon(S_L\rho_L c_L + S_L\rho_I) + (1-\varepsilon)\rho_s c_S - \Delta H_f \varepsilon \rho_I \frac{\partial S_I}{\partial T} \tag{2}$$

where ΔH_f is the latent heat of fusion ($E\cdot M^{-1}$), S_I is the ice saturation, ρ_I is the ice density ($M\cdot L^{-3}$), and c_L, c_I , and c_S are the specific heats of liquid water, ice, and the solid grains, respectively ($E\cdot M^{-1}\cdot °C^{-1}$). The effective thermal conductivity of the matrix is equal to the geometric average thermal conductivity of the matrix constituents and includes the thermal effects of mechanical dispersion:

$$\underline{\underline{\lambda_{eff}}} = \left({\lambda_L}^{S_L} + {\lambda_I}^{S_I}\right)^{\varepsilon} {\lambda_I}^{(1-\varepsilon)} \tag{3}$$

where λ_L, λ_I , and λ_s are the thermal conductivities of liquid water, ice, and grains, respectively (E·t^{-1}·L^{-1}·°C^{-1}). See Table 1 for a full list of required model parameters.

Table 1. Parameters used in Equations 1, 2 and 3.

Parameter	**Symbol**	**Units**
Temperature	T	°C
Temperature of fluid (liquid) source (user-specified value)	T^*	°C
Time	t	s
Porosity (volume of voids per total volume)	ε	1
Liquid-water saturation (volume of unfrozen water per volume of voids)	S_L	1
Ice saturation (volume of ice per volume of voids)	S_I	1
Liquid-water density (user-specified, may be held constant at ~ 1000. [kg/(m^3)] from 0 °C to 20 °C, set to a linear function of temperature, or to a nonlinear function of temperature)	ρ_L	M/L^3
Ice density (user-specified as a constant value, ~ 917. [kg/(m^3)] at 0 °C; ~ 919. [kg/(m^3)] at –10 °C)	ρ_I	M/L^3
Density of solid grain in solid matrix (user specified value, ~ 2600. [kg/(m3)] for typical mineral grains)	ρ_S	M/L^3
Specific heat of liquid (user-specified value, L c ~ 4.182 x 103 [J/(kg·°C)] at 20°C; L c ~ 4.218 x 103 [J/(kg·°C)] at 0 °C)	c_L	E/(M·°C)
Average fluid velocity	$\underline{v}$	L/s
Latent heat of fusion	ΔH_f	E/M
Distributed energy source in liquid (user-specified value)*	γ_L	E/(M·s)
Distributed energy source in solid grains (user-specified value)*	γ_S	E/(M·s)
Fluid mass source (including pure water ma plus solute mass dissolved in source water)	Q_P	M/(L^3·s)
Specific heat of liquid (user-specified value, c_L ~ 4.182 x 103 [J/(kg·°C)] at 20°C; L c ~ 4.218 x 10^3 [J/(kg·°C)] at 0 °C)	c_L	E/(M·°C)
Specific heat of ice (user-specified value, c_I ~ 2.108x10^3 [J/(kg·°C)])	c_I	E/(M·°C)
specific heat of solid grains (user-specified value, c_S ~ 8.4x10^2 [J/(kg·°C)] for quartz or calcite; typical range: 6. to 9. x10^2 [J/(kg·°C)] for other minerals)	c_S	E/(M·°C)
Effective thermal conductivity tensor of the matrix	$\underline{\underline{\lambda_{eff}}}$	E/(t·L·°C)
Fluid thermal conductivity (λ_L~ 0.6 [J/(s·m·°C)] at 20°C; ~ 0.56 J/(s·m·°C) at 0° C)	λ_L	E/(s·L·°C)
Thermal conductivity of ice, user-specified value [user-specified value, ~ 2.14 J/(s·m·°C) at 0°C; ~ 2.3 J/(s·m·°C) at -10°C]	λ_I	E/(s·L·°C)
Thermal conductivity of solid grains, user-specified value [user-specified value, l_S ~ 3.5 J/(s·m·°C) for sandstone at 0°C]	λ_s	E/(s·L·°C)

* Distributed energy sources are energy sources that may occur due to radioactive decay, chemical reactions, or bacterial metabolism, processes not explicitly represented in SUTRA, but their total energy can be included in the energy balance (Voss *et al*., 2017).

2.3 Soil freezing curves

2.3.1 The Clapeyron Equation

The amount of liquid water content in a given soil is important when considering the relative hydraulic conductivity of a frozen soil as it defines the available flow paths (Watanabe & Osada, 2017). Water within the voids of a partially or fully saturated soil freezes *in situ* when the temperature is lowered below the freezing point (T_f) (Andersland & Ladanyi, 1994). However, not all liquid water transforms into ice. Due to soil-water physicochemical interactions, such as capillary forces and the effect of pore curvature, a certain amount of liquid water remains at temperatures below the freezing point, usually considered to be 0 °C (Dash *et al*., 1995). The relationship between unfrozen water content and sub-freezing temperatures (or suction at the ice-water interface, see Figure 2) is known as the soil-freezing characteristic curve (SFCC). Existing parameterizations for the SFCC are based on (1) empirical approaches, which establish the relationships between unfrozen water content and sub-freezing temperature, or (2) physical approaches based on the Clapeyron Equation:

$$\Psi = -\Delta H_f \rho_W \ln \frac{T + 273.15}{T_f + 273.15} \tag{4}$$

where Ψ is suction (kPa); ΔH_f is latent heat of fusion of water (H_f=334,000 J/kg); T is sub-freezing temperature (°C); T_f is normal freezing temperature (T_f = 0 °C); and ρ_W is water density (ρ_W = 1 g/cm^3) (Azmatch *et al*., 2012a; Watanabe *et al*., 2011). The Clapeyron Equation describes the equilibrium relationship between the temperature and pressure in freezing soils. Equation (4) is often simplified into Equation (5) by employing the first term in the Taylor expansion of the exponential function (Kurylyk & Watanabe, 2013; Li *et al*., 2010; Williams, 1964; Zhang *et al*., 2007):

$$\Psi = -L\rho_W \frac{T}{273.15} \tag{5}$$

These Clapeyron formulations ignore the effects of solutes on the SFCC, that lower the freezing point depression (Azmatch *et al*., 2012a). When freezing and thawing processes occur at thermodynamic disequilibrium, the Clapeyron equation is not valid. It should be noted that numerical models that assume thermodynamic equilibrium based on the Clapeyron equation tend to overestimate the rate of ice formation and the amount of water flow from unfrozen to frozen regions (Kurylyk & Watanabe, 2013). Previous studies have utilized an impedance factor to decrease the hydraulic conductivity for frozen soils (e.g., Hansson *et al*., 2004; Jame & Norum, 1980; Lundin, 1990; Zhao *et al*., 1997). However, a decrease in the hydraulic conductivity expressed by the impedance factor has not been experimentally verified. Many researchers have used the generalized Clapeyron equation to model the water retention behaviour of frozen soils (e.g., Azmatch *et al*., 2012a; Dall'Amico, 2010; Hansson *et al*., 2004; Ma *et al*., 2017; Painter & Karra, 2014).

2.3.2 Similarities between SFCC and SWCC

Koopmans and Miller (1966) showed experimentally that SFCCs are similar to soil water retention curves, i.e. soil-water characteristic curves (SWCC), through a scaling relationship between ice pressure (a function of temperature by using the Clapeyron equation) and air pressure (or capillary pressure). The Clapeyron equation can be used to convert sub-freezing temperature to suction or vice versa with assumptions that (i) the pore ice pressure in a saturated frozen soil is equal to atmospheric pressure and (ii) the solute effects are negligible (Ren *et al*., 2017). The analogy between SFCC and SWCC exists due to the similarity in physical processes between drying and wetting in unfrozen unsaturated soil and freezing and thawing in saturated frozen soil. The same sorptive and capillary forces that prevent soil water from draining also prevent it from freezing (Cahn *et al*., 1992). Koopman and Miller's (1966) theory applied to saturated soils that are either free of colloid material (solid-to-solid contact, SS-type, e.g., sand, silt, or coarse clay) or soils in which the particles are always surrounded by water and therefore separated from each other (solid-liquid-solid contact, SLS-type, e.g., suspension in of sodium-saturated montmorillonite clay).

A conceptual SFCC is presented in Figure 2. As temperature decreases and soil suction increases, formation of ice occurs in the largest pores first. The corresponding suction or temperature at this stage is referred to as the ice-entry value (Azmatch *et al*., 2012b). The unfrozen water content in the soil gradually decreases along the freezing curve. At a certain sub-freezing temperature, most of the pore water turns into ice and beyond this temperature extremely low temperatures (i.e., very high suction) would be required to further reduce the unfrozen water. The specific unfrozen water content that remains is referred to as the residual unfrozen water content (S_{WRES}). Similar to SWCC, SFCC can be divided into three zones: boundary effect zone (no pore ice formation), transition zone (sharp drop in the unfrozen water content), and residual zone of unfrozen state (where variation in the unfrozen water content is insignificant despite significant changes in temperature or suction). Like soil drying and wetting, soil freezing and thawing shows hysteretic behaviour, which can be a result of several potential mechanisms such as the effect of electrolytes, solute redistribution, or pore blocking (Watanabe & Osada, 2017).

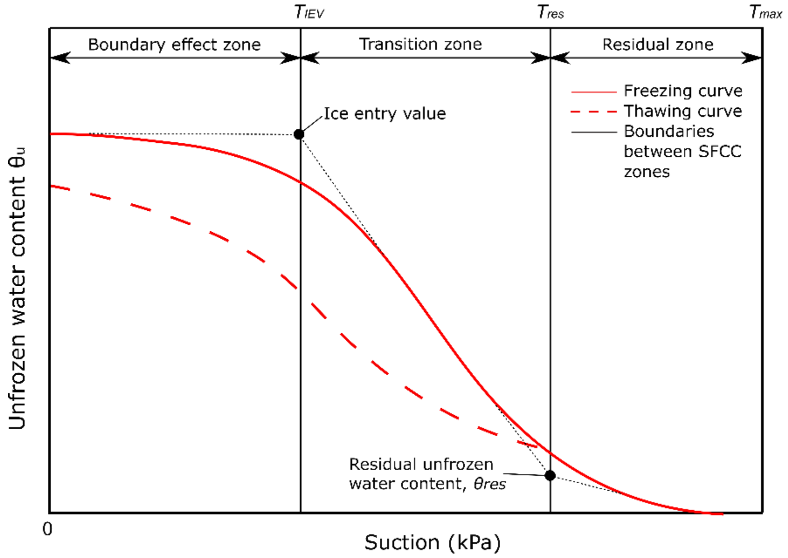

Figure 2. Conceptual soil-freezing characteristic curve. Figure modified from Ren *et al*. (2017).

2.3.3 Overview of existing SFCC expressions

SFCC's not derived from SWCC's

Researchers have derived SFCC expressions independently of any SWCC data based on empirical relationships between the unfrozen water content and sub-freezing temperature (e.g., Anderson & Morgenstern, 1973; Anderson & Tice, 1972; Jame, 1977; Kozlowski, 2007; Kozlowski & Nartowska, 2013; McKenzie *et al*., 2007). If density differences between ice and water are ignored, the total volumetric water content (θ_W) can simply be expressed as the sum of the liquid water content (θ_l) and the ice content (θ_i):

$$\theta_W = \theta_l + \theta_i \tag{6}$$

By assuming unfrozen water content to be independent of total water content, Anderson and Tice (1972) determined the unfrozen water content (θ_l) to be a function of temperature by a simple power curve:

$$\theta_l = \frac{\rho_s(1-\varepsilon)}{100\rho_W}\alpha(-T)^{\beta} \tag{7}$$

where ρ_s is the density of the soil solids (M L^{-3}), ε is the porosity, and α and β are empirical fitting parameters. Because the apparent heat capacity term for freezing/ thawing soils contains the derivative of the SFCC, the SFCC must be smooth and differentiable. The derivative of Equation 4 with respect to temperature is:

$$\frac{\partial\theta_l}{\partial T} = -\frac{\rho_s(1-\varepsilon)}{100\rho_W}\alpha\beta(-T)^{\beta-1} \tag{8}$$

Tice *et al.* (1976) and Andersland and Ladanyi (1994) have tabulated experimental values for α and β for several soils with varying total water contents and different physical properties. Empirical data also demonstrates that the α and β values can be obtained from the specific surface area S (m^2g^{-1}) (Anderson & Morgenstern, 1973; Anderson & Tice, 1972; Blanchard & Fremond, 1985):

$$\alpha = \exp\{0.5519\ \times \ln(S) + 0.2168\} \tag{9}$$

$$\beta = -\exp\{-0.2640\ \times\ \ln(S) + 0.3711\} \tag{10}$$

This indicates that α and β values correspond to basic soil types. For instance, Equation 9 suggests that α is typically higher for soil types with high surface areas such as clay. Tice *et al.* (1976) developed a simple procedure to calculate α and β based on liquid-limit data (defined as the lowest moisture content with a liquid state of consistency (Tuladhar *et al*., 2020)) . The power law parameterization therefore allows the SFCC of a particular soil to be estimated from a few simple laboratory measurements.

Alternatively, Jame (1977) and McKenzie *et al.* (2007) propose a simple piecewise linear function for SFCC:

$$\begin{cases} \theta_l = mT + \theta_W \quad \text{if } T > T_{res} \\ \theta_w = \theta_{res} \quad \text{if } T < T_{res} \end{cases} \tag{11}$$

where m is the slope of the freezing function (T^{-1}), θ_{res} is the residual unfrozen water content, and T_{res} is defined as the temperature at which the linear freezing function attains residual unfrozen water content, θ_{res}.

Kozlowski (2007) achieved a good fit to measured unfrozen water in a clay soil using an exponential piecewise SFCC:

$$\begin{cases} \theta_l = \theta_w \quad \text{if } T > T_f \\ \theta_l = \ \theta_{res} + (\theta_w -\ \theta_{res})\exp\left[\delta\left(\frac{T_f - T}{T - T_{res}}\right)^{\chi}\right] \quad \text{if } T_f > T > T_{res} \\ \theta_l = \theta_{res} \quad \text{if } T \le T_{res} \end{cases} \tag{12}$$

where δ and χ are fitting parameters.

McKenzie *et al.* (2007) and Ge *et al*. (2011) suggest a continuous exponential relationship could also be used to approximate SFCC. Equation 13 is modified such that the porosity is replaced with the total water content to account for unsaturated conditions:

$$\theta_l = \theta_{res} + (\theta_{sat} - \theta_{res})\exp\left[-\left(\frac{T - T_f}{\gamma}\right)^2\right] + \theta_{res}$$

(13)

where θ_{sat} is volumetric unfrozen water content at saturated condition (equal to soil porosity) and γ is a fitting parameter. Both the piecewise linear and exponential SFCC's have smooth derivatives with respect to T on the interval of freezing (McKenzie *et al*., 2007).

In addition to the power, exponential, and non-linear/ linear piecewise relationships, modified versions of the SFCC proposed by Anderson and Tice (1972) have also been used to approximate the relationship between liquid water content and the temperature of freezing soils (e.g., Kozlowski & Nartowska, 2013).

SFCC's derived from SWCC's

The Clapeyron equation allows conversion between SWCC and SFCC by relating suction with sub-freezing temperature. Brooks and Corey (1964), van Genuchten (1980), and Fredlund and Xing (1994) have proposed using SWCC's as SFCC equations by replacing suction at the air-water interface in unsaturated unfrozen soil with suction at the ice-water interface in saturated frozen soil. Using time domain reflectometry, Flerchinger *et al.* (2006) measured liquid water content in freezing soils and found that the SWCC parameters were very similar to SWCC parameters determined from SFCC's directly obtained during freezing tests.

By combining the simplified Clapeyron equation (Equation 5) with the Brooks and Corey (1964) equation, Sheshukov and Nieber (2011) obtained the following relationship:

$$\theta_l = \theta_{res} + (\varepsilon - \theta_{res})\left(\frac{\rho_W L T}{\psi_{IEV} 273.15}\right)^{-1/b}$$

(14)

where ψ_{IEV} is ice-entry value (M L^{-1} t^{-2}) and b is the Brooks and Corey (1964) model parameter. Equation (*14*) is similar to the power relationship proposed in Equation (*7*), however, the Brooks and Corey (1964) model can accommodate sorptive or capillary forces.

Zhang *et al.* (2007) modified a common SFC derived from the Clapp and Hornberger relationship to account for the effect of ice on the soil specific surface:

$$\theta_u = \varepsilon\left(\frac{\rho H_f T}{273.15\psi_{IEV}}\right)^{-\frac{1}{b}}(1 + C_k\theta_i)^2$$

(15)

where b is the empirical Clapp and Hornberger parameter, and C_k accounts for the ice formation effect on matric potential (C_k~8).

Azmatch *et al.* (2012b) showed that the Fredlund and Xing (1994) SWCC could be combined with Clapeyron equation to obtain the following SFCC:

$$\theta_u = \frac{\theta_{sat}}{\left\{\ln\left[2.718 + \left(\frac{L\rho_W}{a_f}\ln\left(\frac{T + 273.15}{T_0 + 273.15}\right)\right)^{n_f}\right]\right\}^{m_f}} \tag{16}$$

where a_f, n_f, and m_f are model parameters from Fredlund *et al.* (1994).

Several modified forms of the van Genuchten (1980) SWCC have also been proposed. Dall'Amico (2010) and Zhang *et al.* (2016) revised the van Genuchten (1980) soil-water curve by incorporating the Clapeyron equation to estimate liquid and ice saturations during freezing. Watanabe *et al.* (2011) combined the Clapeyron equation with the van Genuchten (1980) equation proposed by Durner (1994) to accommodate heterogenous pore structure.

Kurylyk and Watanabe (2013) note that deriving a SFCC by combining existing SWCC's with a form of the Clapeyron equation often makes differentiating the SFCC and its subsequent incorporation into the apparent heat capacity term more difficult. Due to the small time-steps required for unsaturated freezing simulations, the relative complexity of the SFCC derivatives currently limits their use in multi-dimensional or spatially extensive numerical models.

This section provides an overview of a few SFCC formulations and parameterizations, however, there are many modified versions and expressions not listed above that can be used to describe soil freezing. Researchers developing numerical models of cold regions are faced with the challenge of choosing the appropriate type and parameterization of SFCC while balancing model complexity and calibration. Yet there is a lack of understanding whether these factors affect model outcomes and their degree of impact. The purpose of this thesis is to quantify and compare three commonly used SFCCs to better understand how different forms and parametrizations affect physical processes in groundwater models.

3. Methods

3.1 SUTRA modelling equations

I use SUTRA-ice, a modified version of the U.S Geological Survey Saturated-Unsaturated Transport Model. SUTRA-ice is a finite element numerical model that simulates groundwater flow and incorporates the hydrologic and thermodynamic effects of freezing and thawing. SUTRA-ice is modified from the original SUTRA code by changing the spatial properties of the porous matrix that occurs when temperatures at a specific model node or element are below the freezing point, defined as 0 °C in this study. These include the effects of ice on the thermal conductivity, heat capacity, permeability of the porous medium, and the latent heat of formation of ice. Values of thermal conductivity and heat capacity change as a function of ice content and are based on weighted geometric averages of every constituent of the soil matrix (see Section 2.2).

For each timestep, SUTRA-ice calculates pressure and temperature for each node from the governing energy and mass balance equations. The code allows different user-defined functions to describe the freezing of soil. When temperature (T) is above the temperature at which pore water begins to freeze (T_f, defined as 0° C in this study), pore water in the model is entirely in liquid-water form ($S_W = 1$). When temperature is below the freezing temperature, ($T < T_f$), ice can begin to form and SUTRA-ice computes the liquid-water saturation as a function of temperature [$S_W = S_W(T)$]. This study uses and compares three widely used SFCCs under fully saturated conditions (Figure 3). Because SUTRA-ice assumes fully saturated conditions:

$$S_W^{sat} + S_I^{sat} = 1 \tag{17}$$

where S_W^{sat} and S_I^{sat} are the saturation of liquid water and ice respectively.

The first SFCC is a simple piecewise linear function (blue curve in Figure 3a):

$$S_W^{sat} = \begin{cases} 1 & \text{for } T \geq T_f \\ (1 - S_{Wres})\left(\dfrac{T - T_{Wres}}{T_f - T_{Wres}}\right) + S_{Wres} & \text{for } T_{Wres} < T < T_f \\ S_{Wres} & \text{for } T \leq T_{Wres} \end{cases} \tag{18}$$

where $S_W^{sat}$is the total water saturation, S_{Wres} is the residual (minimum) liquid water saturation, and T_{Wres} is the user-defined temperature at which S_{Wres} occurs. Differentiation of Equation (18) with respect to T (blue curve in Figure 3b) gives:

$$\frac{dS_W^{sat}}{dT} = \begin{cases} 0 & \text{for } T \geq T_f \\ \dfrac{1 - S_{Wres}}{T_f - T_{Wres}} & \text{for } T_{Wres} \leq T \leq T_f \\ 0 & \text{for } T < T_{Wres} \end{cases} \tag{19}$$

The second function is the exponential liquid-water saturation function (orange curve in Figure 3a), adapted from Mottaghy and Rath (2006):

$$S_W^{sat} = \begin{cases} 1 & \text{for } T \geq T_f \\ (1 - S_{Wres})\exp\left\{-\left(\dfrac{T - T_f}{w}\right)^2\right\} + S_{Wres} & \text{for } T < T_f \end{cases} \tag{20}$$

where w is the user-defined fitting parameter ($w > 0$). Differentiation of Equation (20) with respect to T (orange curve in Figure 3b) gives:

$$\frac{dS_W^{sat}}{dT} = \begin{cases} -(1 - S_{Wres})\left(\frac{2}{w}\right)\left(\frac{T - T_f}{w}\right) exp\left\{-\left(\frac{T - T_f}{w}\right)^2\right\} \text{for } T < T_f \\ \qquad\qquad 0 \text{ otherwise} \end{cases} \tag{21}$$

The third soil-freezing function relates the liquid-water saturation to the temperature in accordance with a power law (green curve in Figure 3a) (Anderson & Morgenstern, 1973; Anderson & Tice, 1972):

$$S_W^{sat} = \begin{cases} 1 \text{ for } S_i^{sat} < 0 \\ \alpha_{POW}(T_f - T)^{\beta_{POW}} \text{ for } T < T_f \end{cases}$$
$$S_W^{sat} \geq S_{Wres} \tag{22}$$

where α_{POW} and β_{POW} are user-specified power law model parameters ($\alpha_{POW} > 0$; $\beta_{POW} < 0$). Differentiation with respect to T (green curve in Figure 3b) leads to:

$$\frac{\partial S_W^{sat}}{\partial T} = \begin{cases} 0 \text{ for } T \geq T_f \\ -\alpha_{POW}\beta_{POW}\left(T_f - T\right)^{\beta_{POW}-1} \text{ for } T < T_f \end{cases}$$

(23)

The permeability, *k* (L^2), of ground that is frozen and/or unsaturated decreases as ice forms in pore spaces. This decrease can be represented with an impedance function (McKenzie *et al*., 2007):

$$k = k_{sat}10^{-\Omega(1-S_L)}$$

(24)

where $k_{sat}$is the permeability of the unfrozen saturated ground (L^2) and Ω is the impedance factor.

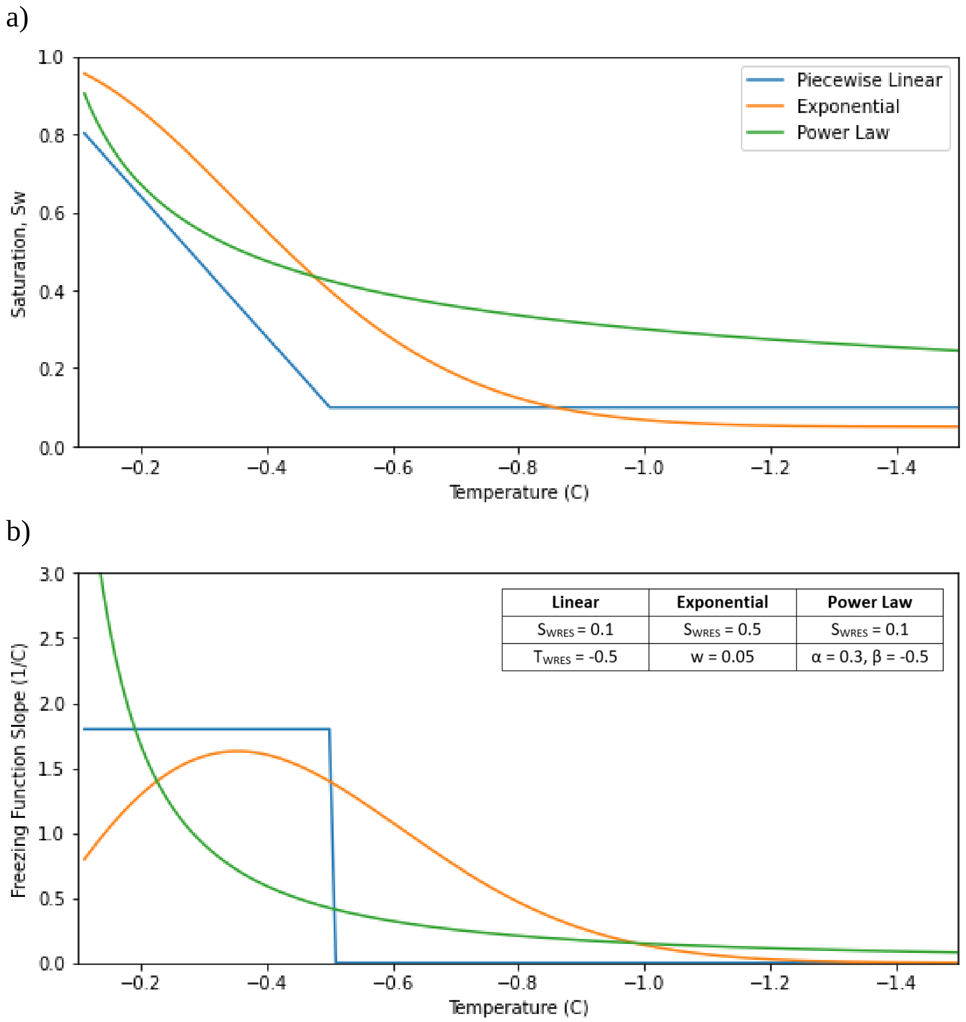

Linear	Exponential	Power Law
S_{WRES} = 0.1	S_{WRES} = 0.5	S_{WRES} = 0.1
T_{WRES} = -0.5	w = 0.05	α = 0.3, β = -0.5

Figure 3. (a) Examples of piecewise linear (Eq. 16), exponential (Eq, 18), and power law (Eq. 20) freezing functions and (b) the slopes of the functions. Inset table shows the parameters used for the three functions.

Table 2. Model parameters used for the freeze/thaw simulations.

Parameter	**Unit**	**Value**
Ice		
Specific heat, c_I	J/(kg°C)	2108
Thermal conductivity, λ_I	W/(m°C)	2.14
Density, ρ_I*	kg/m^3	920
Latent heat of fusion, ΔH_f	J/kg	334,000
Liquid water		
Specific heat, c_L	J/(kg°C)	4182
Thermal conductivity, λ_L	W/(m°C)	0.6
Density, ρ_W	kg/m^3	1000
Compressibility, β_L	ms^2/kg	4.47×10^{-10}
Solid matrix		
Specific heat, c_S	J/(kg°C)	840
Thermal conductivity, λ_S	W/(m°C)	3.5
Horizontal permeability at saturation, k_H	m^2	1×10^{-13}
Vertical permeability at saturation, k_V	m^2	1×10^{-14}
Compressibility, α	ms^2/kg	1×10^{-8}
Density, ρ_S	kg/m^3	2600
Porosity, ε	-	0.1
Other		
Gravity, $\underline{g}$	m/s^2	-9.81
Longitudinal dispersivity of solid matrix, α_L	m	0.5
Transverse dispersivity of solid matrix, α_T	m	0.5
Permeability function (Equation 24)		
Impedance factor, Ω **	-	5.4
Thermal boundary layer above ground surface		
Heat transfer coefficient***	J/sm^2°C	1.25
Height	m	1
Freezing function	-	None
Permeability, $\underline{\underline{k}}$	m^2	10^{-40}
Specific heat, c_s	J/kg	0
Solid grain thermal conductivity, λ_S	J/sm°C	1.25
Porosity, ε	-	Top = 1×10^{-5} Bottom = 0.1
Bottom boundary geothermal heat flux		
Energy source	(J/s)/m^2	0.085

* From McKenzie *et al.* (2007)

** To fit with the minimum permeability from Evans & Ge (2017)

*** From McKenzie & Voss (2013)

3.2 Model development and configuration

3.2.1 Model domain and mesh

The model is a two-dimensional cross-section representative of a simple permafrost landscape where groundwater discharges into a downgradient river. The total length of the model domain is 250 m, with the last 10 m of the model representing half of a triangular river channel with a 50% land surface slope. The 240 m land surface has a slope of 2%. The model is 55 m thick upslope (left vertical boundary) and 45.2 m downslope (right vertical boundary). The domain is divided into 4 horizontal bands with varying element sizes in the y-direction, from 0.2 m at the land surface to 2 m at the bottom boundary. The model domain is comprised of 12038 nodes and 11740 elements. The width of the elements (x-direction) is 1 m for the entire domain. Preliminary tests by Lamontagne-Hallé (*in preparation*) show that the mesh discretization used in this study provides accurate results while limiting computational time, and using a finer mesh does not significantly affect model results. The intrinsic properties of every phase (i.e., soil particles, liquid water, and ice) are homogenous, excluding the surface thermal boundary layer (see Section 3.2.2). A horizontal and vertical permeability is 10^{-13} and 10^{-14} m^2 respectively, for an 1:10 anisotropy ratio.

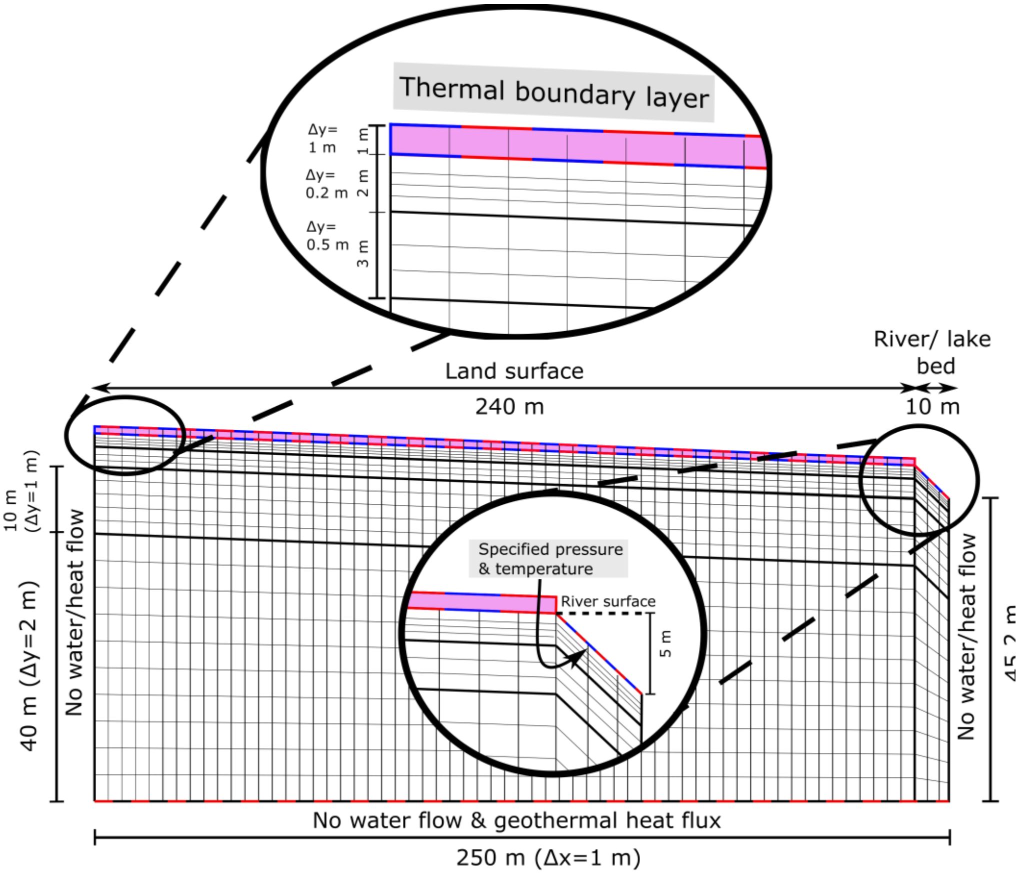

Figure 4. Model configuration and mesh discretization, including a 1-meter-thick thermal boundary layer (pink). Dashed lines show boundaries where water (blue) and heat (red) are flowing into or out of the model domain. The actual mesh is 2x denser than displayed in the figure.

3.2.2 Boundary conditions

The vertical boundaries of the model correspond to watershed divides with no water flow or heat flux. The bottom horizontal edge is defined as a no-flow geologic boundary and a specified heat flux of 0.085 W/m^2 to represent the geothermal heat gradient (McKenzie & Voss, 2013). The 240 m land surface on the upper boundary is represented by a combination of hydraulic drain, specified recharge, and specified heat flux boundary conditions. The groundwater recharge boundary is a function of the time of year and climatic conditions (air temperature, summer precipitation, and winter precipitation). The seasonal specified recharge has 3 stages. First, when air temperature is below 0°C, there is no recharge and winter snow accumulates on the land surface. In the second stage, when air temperature exceeds 0°C, recharge rapidly increases for 15 days. Recharge during this stage (i.e., spring freshet) comes from both summer precipitation and snowmelt. The peak value of recharge is proportional to the amount of snow accumulated during the previous stage (<0°C, below freezing season). In the 15 days following this peak, recharge decreases linearly until there is no snowpack left (simulating freshet). In the last stage, following freshet, the ratio of summer precipitation recharging the model is 0.2 (i.e., runoff ratio of 0.8). The cycle repeats once air temperature decreases below 0°C. The values of 64.75 mm/month are used for summer precipitation and 17.60 mm/month for winter precipitation. These values are calculated from meteorological data measured in Beaver Creek, Yukon, Canada. Beaver Creek, an area underlain with discontinuous permafrost, has been the subject of multiple road stabilization and permafrost degradation studies (e.g., Chen *et al*., 2016; de Grandpré *et al*., 2012; Stephani *et al*., 2014).

Applying a surface drain boundary condition on the upper boundary of the model allows water from surface nodes with a pressure greater than 0 Pa to be removed from the model domain. The amount of water that is discharged at the surface depends on the simulated pressure at the node. Using a specified recharge with a drain boundary condition prevents an unrealistic amount of recharge from being forced into the surface of the model and defines the maximum available water for recharge. Groundwater is allowed to discharge (exit) or recharge (enter) anywhere along the land surface when ice is not blocking flow.

A 1-meter-thick thermal boundary layer is applied along the land surface, underneath the specified air temperature boundary and above the specified recharge/drain boundary condition. The thermal boundary layer acts as a buffer zone and represents the exchange of energy between the air and ground surface. This layer is defined with a thermal conductivity of 1.25 J/sm°C (based on calibrated field measurements from McKenzie *et al.* (2007)), a permeability of 10^{-40} m^2 (essentially zero), and zero heat capacity, thus no water flow or freezing occurs through the thermal boundary layer. The specified air temperature boundary condition is defined by a sinusoidal function fitted with the observed air temperature measured in Beaver Creek from 2008 to 2018 (R^2 of 0.979; Figure 5):

$$T_{air} = x - \left[y \sin\left(\frac{2\pi t}{365.25}\right)\right] \tag{25}$$

where T_{air} is the average daily air temperature, x is the annual average air temperature (–3.6°C), y is the seasonal temperature amplitude (18.8°C), and t is time in days. Using a synthetic function based on averages allows us to reproduce observed seasonal parameters while ensuring model stability. Results from Lamontagne-Hallé *et al.* (*in preparation*) show that using this sinusoidal function, instead of directly measured air temperatures, does not affect model results.

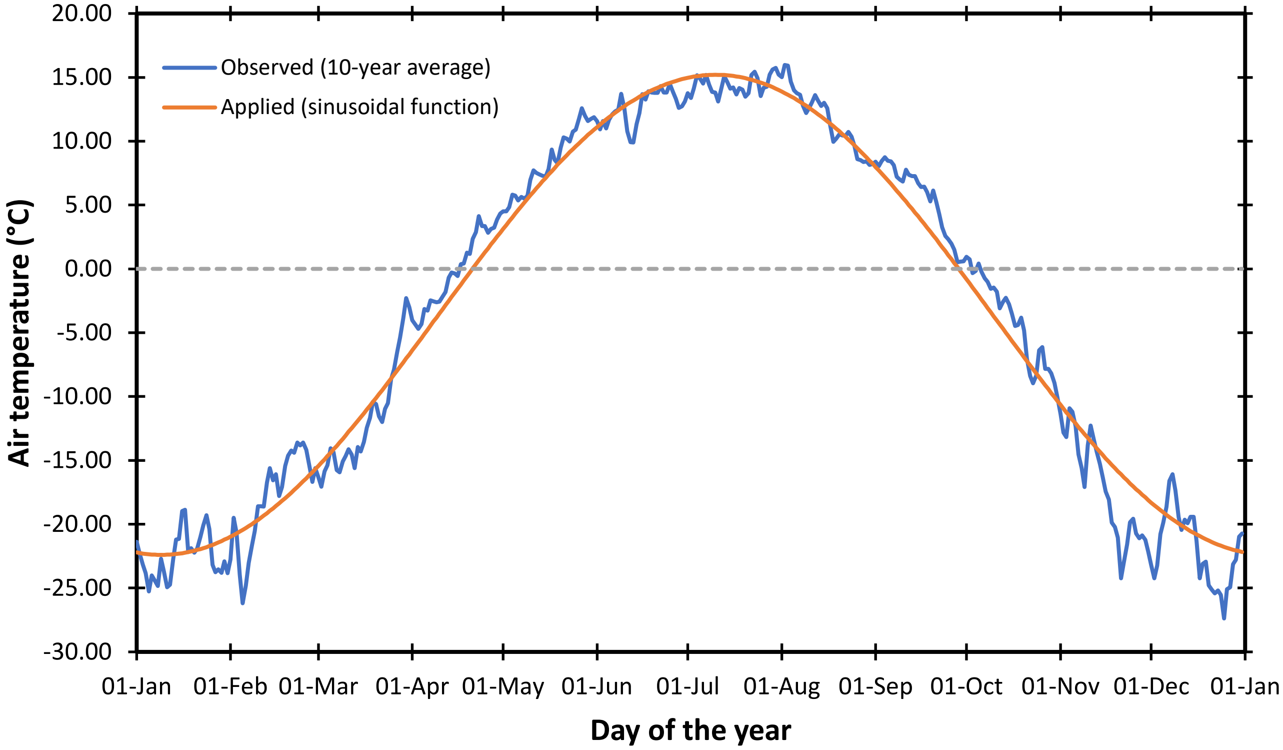

Figure 5. Average observed air temperatures for each day of the year from 2008 to 2018 in Beaver Creek (blue line) and the sinusoidal function representing the air temperature boundary condition at the land surface (orange line).

3.3 Modelling sequence

Each simulation was run in three phases. The first two phases were sequential spin-ups to generate initial conditions (as described by Lamontagne-Hallé *et al.* (*in preparation*)). The first phase produces the starting pressure and temperature distribution across the model. To generate hydrostatic pressure, the surface nodes are set to a specified temperature of 5°C and a specified pressure of 0 Pa. The ground temperature at the surface is decreased -0.01°C per year for 860 years, until it reaches –3.6°C (the mean annual air temperature measured at Beaver Creek from 2008 to 2018). The model is then run for 10,000 years with a constant temperature of –3.6°C at the land surface to generate a stable temperature distribution.

The second phase is a seasonal spin-up that forms an active layer and a stable water pressure distribution in the shallow supra-permafrost layer. This phase is run for 100 years with 2-hour timesteps. The air temperature follows the sinusoidal function described in Section 3.2.2 and Equation 25. The third phase produces model results that are then analyzed and compared. Each simulation is run for 10 years with 2-hour timesteps, with a sinusoidal air temperature function (Figure 5). Running the simulation for 10 years allows the model to reach dynamic equilibrium, meaning there is no significant difference in the model outcomes year to year by year 10.

To compare different parameterizations of each SFCC, multiple simulations were run with various S_{WRES} and T_{WRES} values for piecewise linear, S_{WRES} and w parameter values for exponential, and α and β values for power function. Residual saturation (S_{WRES}) values ranged between 0.01 and 0.5 for piecewise linear and power law SFCC's, and between 0.01 and 0.1 for exponential SFCCs (only 3 S_{WRES}

values were tested for the exponential function due to limitations in fitting experimental data to $S_{WRES} > 0.1$). For each S_{WRES} value, multiple temperature ranges of freezing (T_{WRES} values) between –0.5°C and –10°C were tested. A total of 20 simulations were run using piecewise linear, 12 simulations using exponential, and 5 simulations for the power law function (Table 2). Repeated nonlinear least-squares optimization of 417 experimental soil datasets produced the *w* parameter values used for the exponential function and the α and β values for the power law function fitted to the same temperature ranges of freezing used in the piecewise linear simulations (see Appendix).

Table 3. SFCC test parameters. For each simulation, unique combinations of SWRES and TWRES were selected to test all combinations in this table

	Piecewise linear	**Exponential**	**Power law**
$\mathbf{S_{WRES}}$ (residual saturation of water)	0.01	0.01	0.01
	0.05	0.05	0.05
	0.1	0.1	0.1
	0.25		0.25
	0.5		0.5
$\mathbf{T_{WRES}}$ (temperature at which residual liquid saturation, S_{WRES}, is reached)	-0.5°C	-0.5°C	*
	-2°C	-2°C	
	-5°C	-5°C	
	-10°C	-10°C	

*The power law freezing function does not use T_{WRES} values. The shape of the power law function is controlled only by the α, β, and S_{WRES} parameters.

4. Results and Discussion

4.1 Groundwater and ice storage patterns

4.1.1 Water saturation

Figures 6 to 8 show vertical heatmaps representing water saturation values taken from the middle of the model (x = 125 m). Maximum values of 1 (dark blue) indicate areas that are fully saturated with liquid water while values closer to 0 (white) represent higher ice saturation. The average depth to the permafrost (orange line) is calculated using linear interpolation between model nodes to determine the point where ground temperature exceeds 0 °C.

For piecewise linear simulations, decreasing the T_{WRES} or increasing the S_{WRES} value (while keeping the other parameter constant) results in a model with less ice-saturation which means that both variables independently change the hydrogeological regime. For simulations with S_{WRES} of 0.01 (Figure 6a), the ground is fully frozen with a seasonal thawing front for higher values of T_{WRES} (Figure 21, Scenario A). The mushy zone (*i*.e., where both ice and liquid water coexist) that forms at the interface between the thawing front and permafrost is wider when T_{WRES} is –2 °C compared to –0.5 °C. For T_{SWRES} values lower than –2 °C, only the upper 10-15 m of the model is frozen in the winter. At greater depths the ground is perennially thawed, allowing for deeper groundwater flowpaths (Figure 21, Scenario C). Using a S_{WRES} value of 0.5 results in unfrozen ground year-round in the upper and lower sections of the model (Figure 6b), with lower T_{WRES} corresponding to a more liquid water-saturated model. A higher freezing point depression (higher T_{WRES} values) limits the heat dissipation by increasing the slope of the SFCC thus changing the rate of phase change inducing a slower freezing front propagation. The depth to permafrost and the depth of the thawing front increases with wider temperature ranges of freezing (lower T_{WRES} values) and higher S_{WRES} values. For S_{WRES} of 0.01, the average permafrost depth is 2.38 m for T_{WRES} of –0.5 °C and 2.82 m for T_{WRES} of -10°C. Increasing the S_{WRES} value while keeping T_{WRES} constant at a value of -10°C increases the average permafrost depth by 0.7 m and 0.84 m when T_{WRES} is kept constant at –0.5 °C.

Simulations of water and ice saturation with the power law SFCC (Figure 7) follow a similar pattern as the piecewise linear, where increasing S_{WRES} results in models with less ice-saturation. The degree of ice saturation is similar for both piecewise linear and power law simulations with low S_{WRES} (Figure 21, Scenario A). For power law simulations with a high S_{WRES}, the ground remains water-saturated even in the winter (Figure 21, Scenario B). The depth to permafrost increases from 2.53 m for S_{WRES} of 0.01 to 3.08 m for S_{WRES} of 0.5.

Figure 8 shows changing the S_{WRES} and T_{WRES} values for simulations using the exponential freezing function has little to no effect on the water/ice saturation distribution. Like piecewise linear simulations with S_{WRES} of 0.01 and T_{WRES} of –0.5 °C, the model is fully frozen in the winter and thawed from the top down in the summer (Scenario A). The depth to the permafrost table also does not change significantly with S_{WRES}.

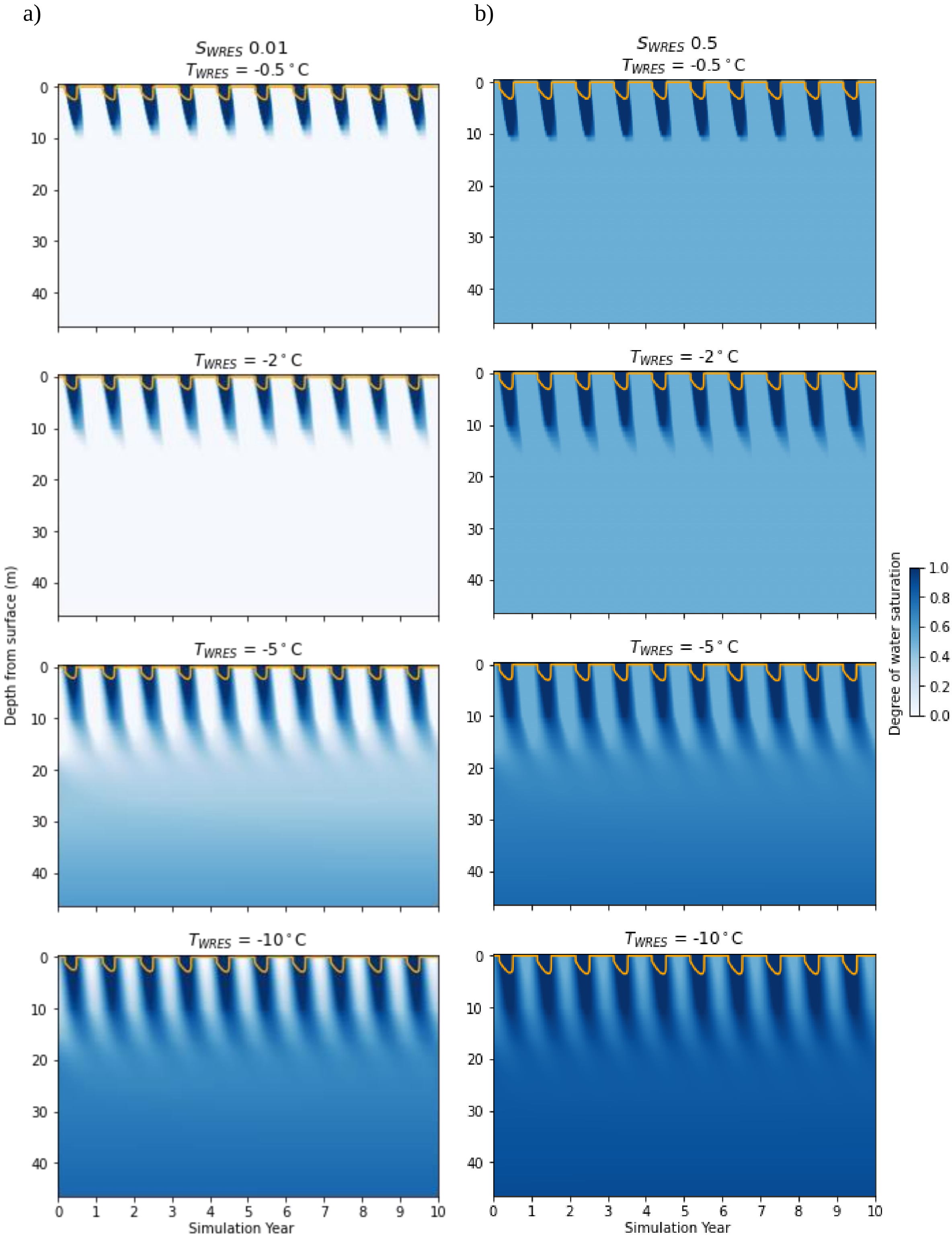

Figure 6. Liquid water saturation profiles for simulations using piecewise linear freezing functions with (a) S_{WRES} of 0.01 (lowest value tested) and (b) S_{WRES} of 0.5 (highest value tested). The depth to the permafrost layer is represented by the orange line.

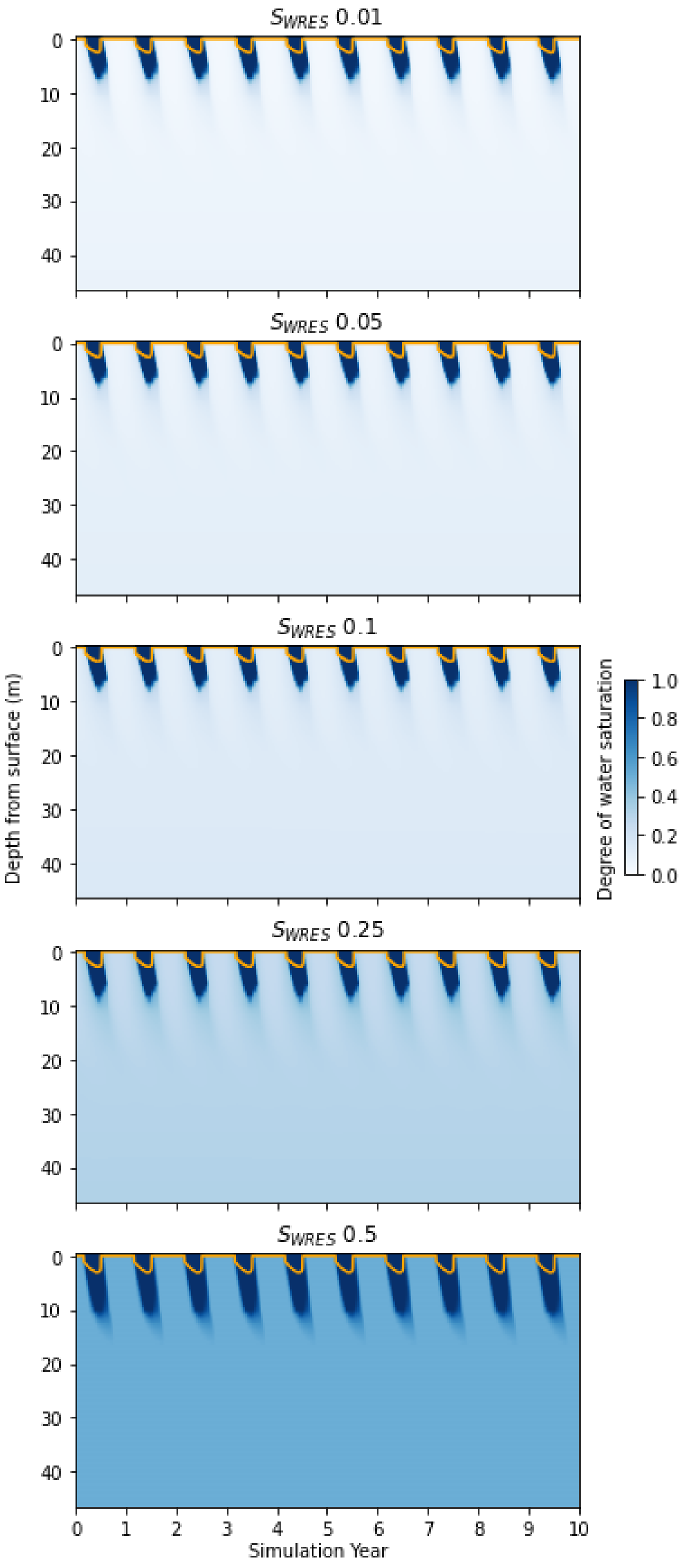

Figure 7. Water saturation profiles for simulations using a power law freezing function with S_{WRES} values ranging from 0.01 (lowest value tested) to 0.5 (highest value tested). The depth to the permafrost layer is represented by the orange line.

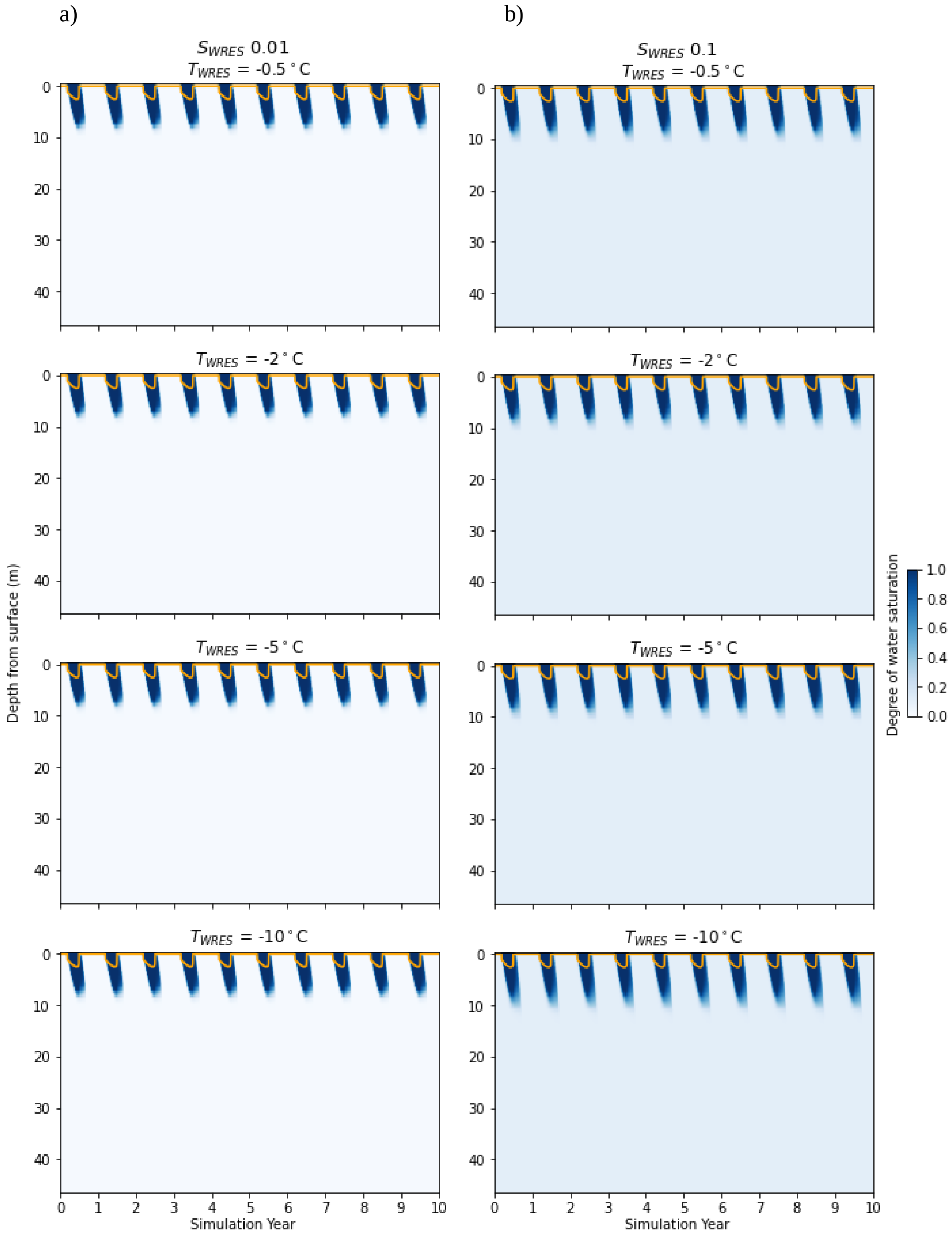

Figure 8. Water saturation profiles for simulations using exponential freezing functions with (a) S_{WRES} of 0.01 (lowest value tested) and (b) S_{WRES} of 0.1 (highest value tested). The depth to the permafrost is represented by the orange line.

These results demonstrate that the type and parameterization of SFCC significantly influences the degree and distribution of ground ice and water saturation, and by association the hydraulic conductivity in the models. In general, using a low S_{WRES} value (e.g., 0.01 or 0.05) combined with a high T_{WRES} value (excluding the power law function, which does not use a T_{WRES} parameter) leads to a model that forms more permafrost and a seasonally thawed active layer. A soil-freezing curve with a lower residual water content at higher temperatures describes a SFCC with a steep phase change slope, meaning a high rate of freezing with negative temperatures. With the exception of the exponential freezing function, using a SFCC with a high S_{WRES} or low T_{WRES} results in ground that is only partially frozen and more water saturated in winter because the rate of freezing is slower and there is more liquid water that is forced to remain. The exponential SFCC curve does not differ with changing parameterization, suggesting that the shape of the function is relatively similar for each parameterization.

4.1.2 Total ice content

Figures 9 to 11 show the difference in total ice content in the last two years of each simulation, normalized to the maximum volume of ice.

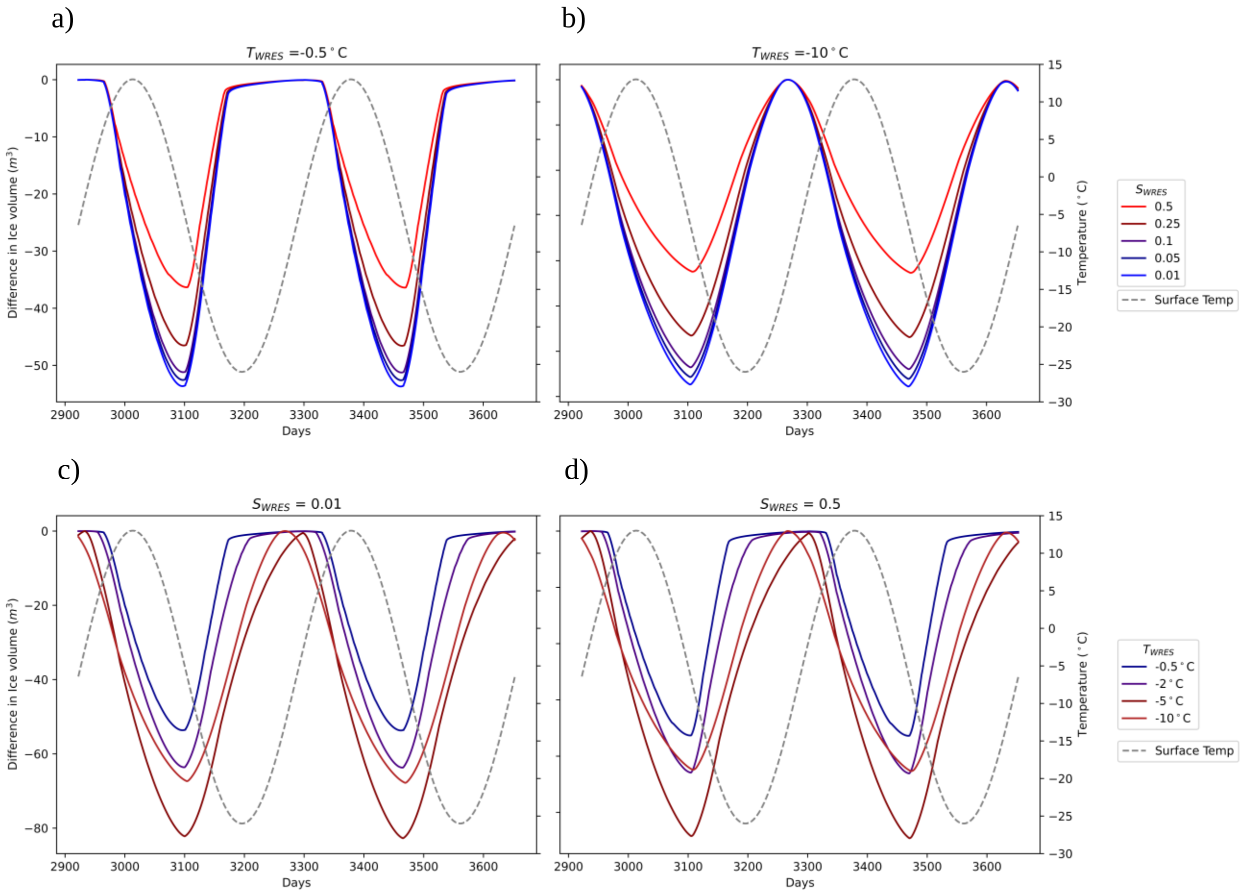

Figure 9. Difference in total ice volume over the last two years for piecewise linear simulations with (a) T_{WRES} = –0.5 °C, (b) T_{WRES} = –10 °C, (c) S_{WRES} = 0.01, and (d) S_{WRES} = 0.5.

Figure 9 shows the change in total ice content in the last two years for simulations where T_{WRES} is kept constant at –0.5 °C and –10 °C while S_{WRES} is systematically changed (Figure 9*a* and *b*), or where S_{WRES} is kept constant at 0.01 and 0.5 while T_{WRES} is systematically changed (Figure 9*c* and *d*). For piecewise linear simulations with a high T_{WRES} value (Figure 9*a*), the ice volume reaches its maximum in winter and stays nearly constant (slight increase due to ice forming near the talik or mushy zone under the river) until seasonal thaw begins, suggesting a stable permafrost system. Conversely, the ice volume in simulations with a low T_{WRES} value (Figure 9*b*) does not peak and plateau in winter but instead reaches a maximum point in the spring and then begins to thaw immediately, indicating a degrading permafrost system. For both high and low T_{WRES} values, decreasing S_{WRES} leads to greater differences in ice volume in the spring and summer as models with high S_{WRES} are water-saturated year-round. A similar pattern is observed when T_{WRES} is decreased from –0.5 °C to –10 °C while S_{WRES} is kept constant (Figure 9*c* and *d*). A smaller temperature range for phase change (e.g., T_{WRES} of –0.5 °C) induces a steeper freezing function and requires a higher amount of latent heat absorbed for one time step. The propagation of the 0 °C isotherm is slower than with larger temperature ranges (e.g., T_{WRES} of –10 °C) because the latent heat fluxes are greater than the conductive fluxes from the surface. The amount of latent heat required is larger at the surface because the temperature profile is steepest here.

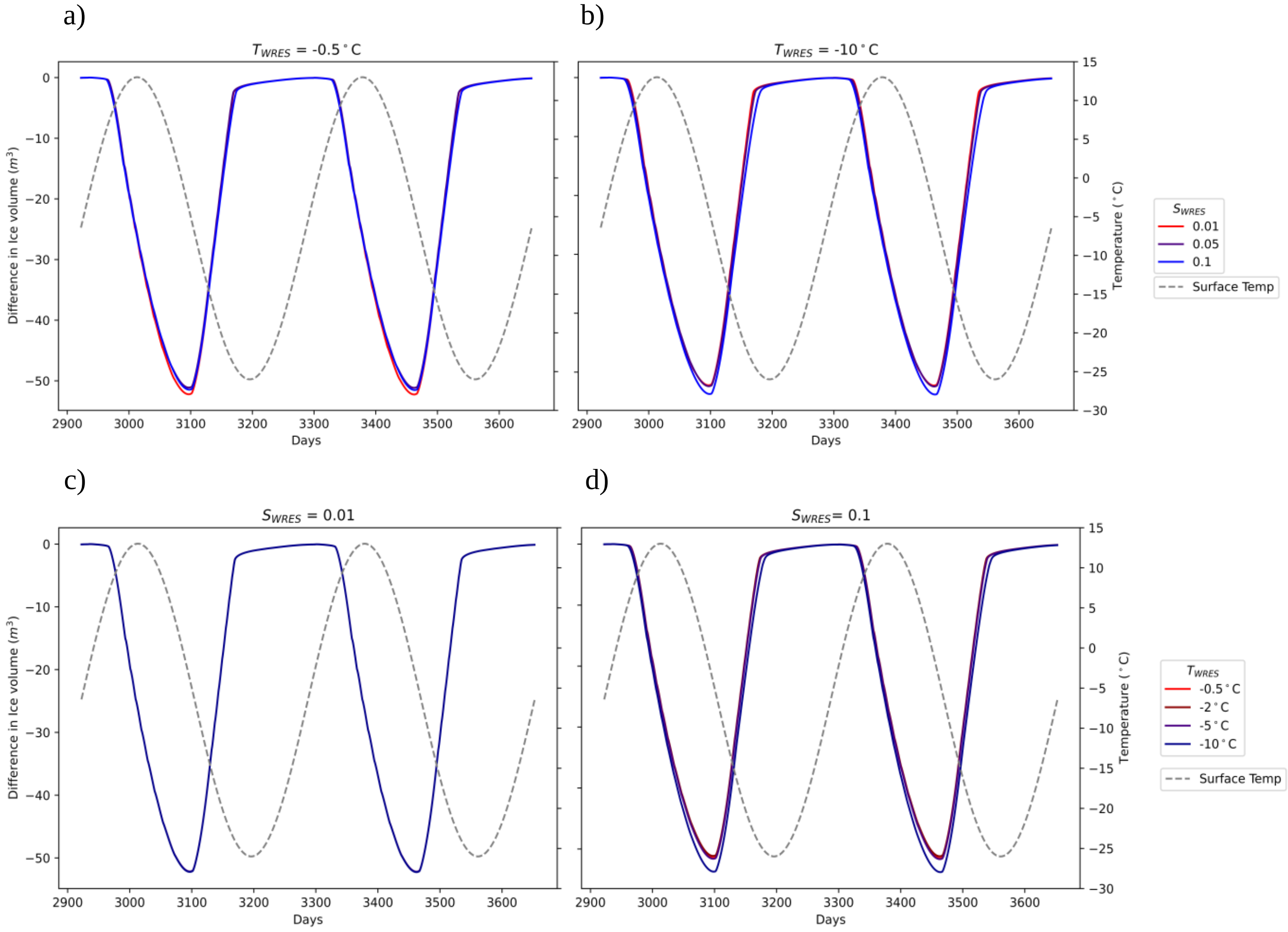

Figure 10. Difference in total ice volume over the last two years for exponential simulations with (a) T_{WRES} = –0.5 °C, (b) T_{WRES} = –10 °C, (c) S_{WRES} = 0.01, and (d) S_{WRES} = 0.1.

A stable permafrost system is observed for all simulations using the exponential SFCC (Figure 10). Because the model is completely frozen in the winter and has a similar active layer and thawing front depths for each simulation, the patterns of changing ice content are nearly identical for all S_{WRES} and T_{WRES} combinations. The exponential simulations have more ice content overall compared to the piecewise linear simulations with the same S_{WRES} and T_{WRES} values (Figure 11). The difference in ice volume between these two types of freezing curves increases with wider temperature ranges of freezing. Using a larger freezing point depression (e.g., T_{WRES} = –0.5 °C or –2 °C) for both the piecewise linear and exponential SFCC will result in a permafrost model with a seasonally thawed active layer. However, a piecewise linear SFCC with a high freezing point depression (e.g., T_{WRES} = –5 °C or –10 °C) does not form permafrost or seasonally frozen ground, unlike the exponential SFCC that forms the same volume of ice for all temperature ranges of freezing.

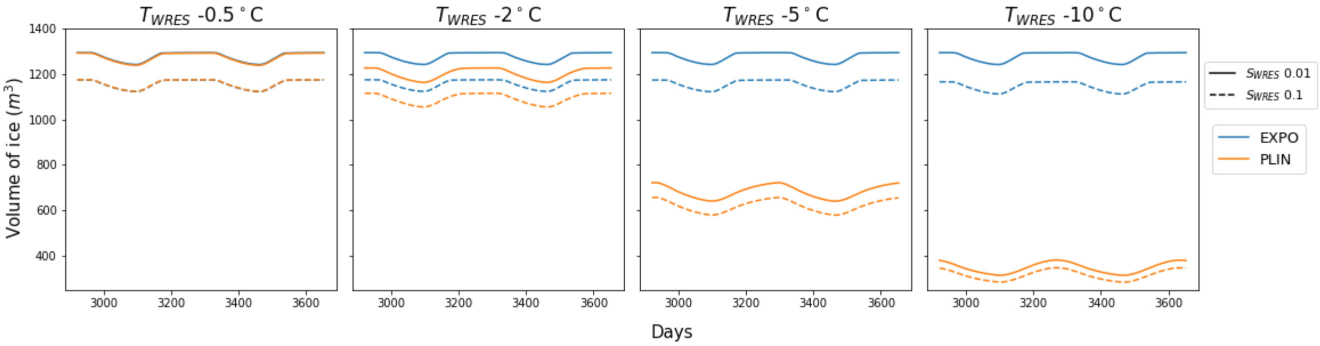

Figure 11. Ice volume in the last two years of piecewise linear (‘PLIN’, orange line) and exponential (‘EXPO’, blue line) simulations. The solid lines represent S_{WRES} of 0.01 and the dashed lines represent S_{WRES} = 0.1. For T_{WRES} of –0.5 °C, the ice volumes for the piecewise linear and exponential simulations are nearly identical (blue and orange lines overlap).

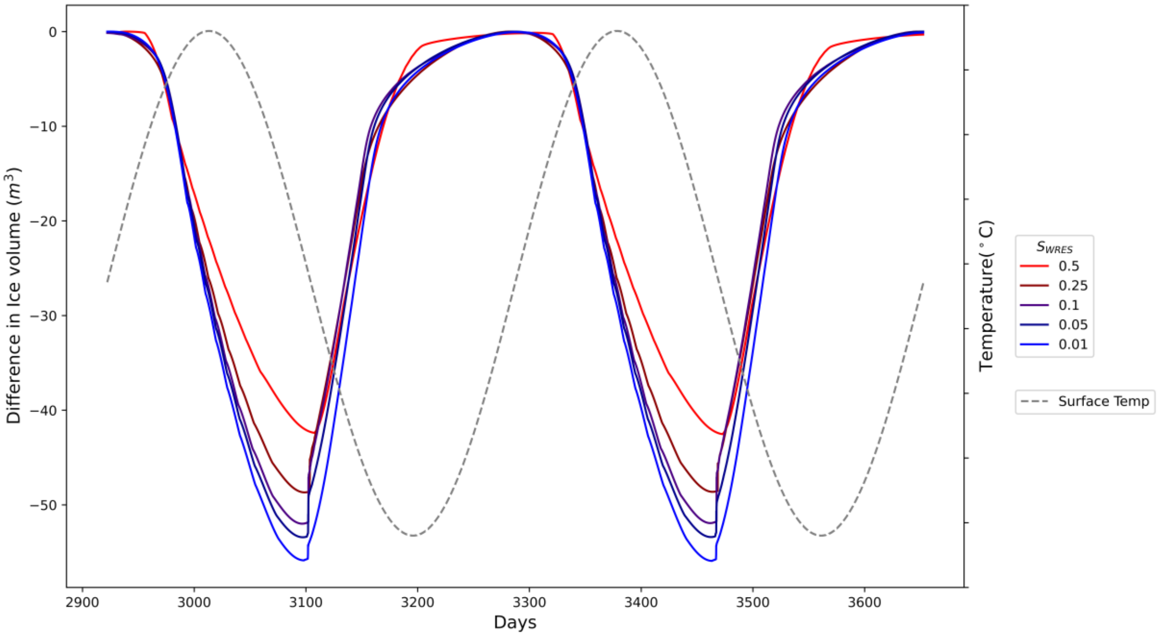

Figure 12. Difference in total ice volume over the last two years for each power law simulation.

For power law simulations, the seasonal change in ice pattern suggests a semi-stable permafrost system (Figure 12). The red line in Figure 12 (S_{WRES} of 0.5) reaches a maximum ice volume and essentially plateaus, suggesting that a higher S_{WRES} value will lead to a more stable permafrost system. Similar to the piecewise linear simulations, lower S_{WRES} values lead to larger differences in ice volume due to permafrost formation and seasonal thaw. The maximum total volume of ice for power law simulations is 1230 m^3 for S_{WRES} of 0.01 and 626 m^3 for S_{WRES} of 0.5, which is slightly less compared to equivalent piecewise linear simulations (1293.16 m^3 for S_{WRES} of 0.01 and T_{WRES} of -0.5 °C; 653.12 m^3 for S_{WRES} of 0.5 and T_{WRES} of –0.5 °C) and exponential simulations (1295.01 m^3 for S_{WRES} of 0.01 and T_{WRES} of –0.5 °C; 1174.81 m^3 for S_{WRES} of 0.1 and T_{WRES} of –0.5 °C).

4.2 Temperature profiles

Figures 13 to 18 plot temperature ‘envelope’ profiles that illustrate the maximum and minimum ground temperatures with depth taken from the middle of the model (x = 125 m). Mean ground surface temperature (–1.9 °C) can be obtained by extrapolating the overlaping lines of the maximum and minimum profiles to the horizontal axis (black dotted line in Figures 13 to 16). The intersection of the ground thermal profile in summer (right-hand component of the temperature envelope) with the 0 °C vertical line defines the depth of the active layer.

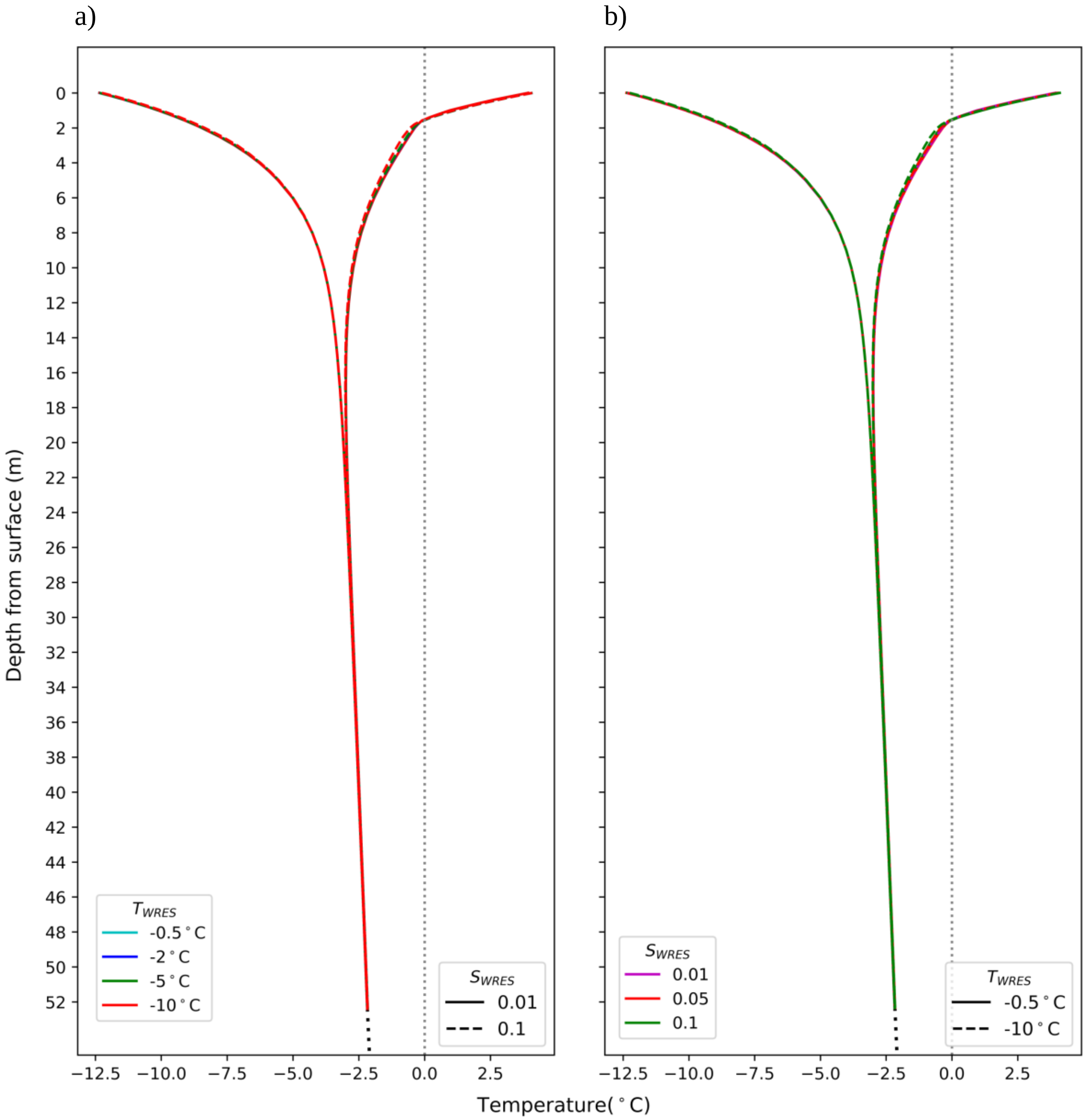

Figure 13. Temperature profiles for models using an exponential freezing function with (a) constant S_{WRES} or (b) constant T_{WRES}.

Figure 13 demonstrates how changing the T_{WRES} or S_{WRES} value for exponential simulations does not affect the thermal profile of the model. The thickness of the active layer and the depth (and value) of 0 annual amplitude (level at which no significant seasonal temperature fluctuations occur) is the same for each simulation.

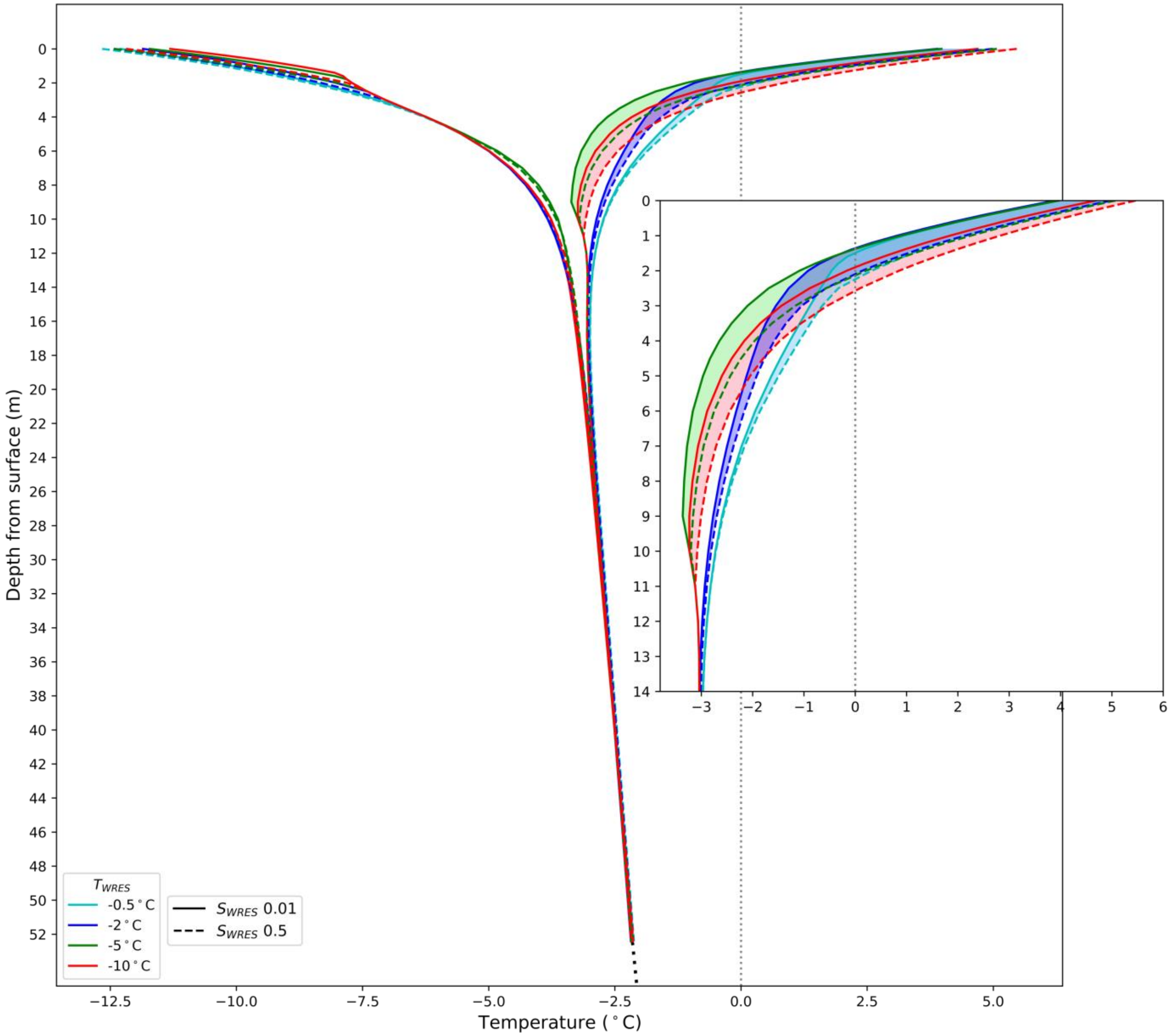

Figure 14. Ground temperature profiles for piecewise linear simulations using a low S_{WRES} value (solid lines) or high S_{WRES} value (dashed lines). 0°C is represented by a grey vertical dotted line. The inset figure shows maximum temperatures for the upper 14 m of the model.

Figure 14 compares temperature profiles for models using a piecewise linear SFCC. The shaded regions in between the solid and dashed lines illustrate changes in the temperature profiles when increasing S_{WRES} values from 0.01 to 0.5. The simulations using a high S_{WRES} value (dashed lines) are warmer at greater depths compared to simulations using a low S_{WRES} value (solid lines) because less energy is used in phase change. Simulations using a piecewise linear freezing function with a high S_{WRES} have low ice content even in winter, meaning there is less latent heat required for complete thaw (faster thawing front) and more thermal energy can be used to heat the subsurface. A higher S_{WRES} value results in a deeper active layer, for example, the difference in depth for the two dashed and solid lines for T_{WRES} = –0.5 °C is approximately 0.7 m. This is approximately 6 – 9 % of the total thaw depth – a significant potential source of error.

Due to the mushy zone beneath the thawing front, the maximum temperatures of the T_{WRES} = –5 °C and T_{WRES} = –10 °C thermal profiles change slope steepness approximately 9-10 meters from the surface. The inset on Figure 14 shows the relatively complicated behaviour of the system at this depth. The model remains in phase change as there is insufficient heat to completely thaw out the mushy zone for T_{WRES} of –5 °C and –10 °C simulations with S_{WRES} of 0.01. The freezing function with T_{WRES} = –10 °C has a wider freezing range than T_{WRES} = -5 °C thus the specific heat needed to heat the mushy zone is incrementally less. The maximum temperatures for the T_{WRES} = –0.5 °C temperature profile is warmer than the –2 °C profile as the –0.5 °C model is completely frozen and the thermal conductivity of ice is greater than the thermal conductivity of water. Because the –0.5 °C model is fully frozen, heat is conducted downwards relatively easier compared to the –2 °C model which has only has partially frozen ground at this depth.

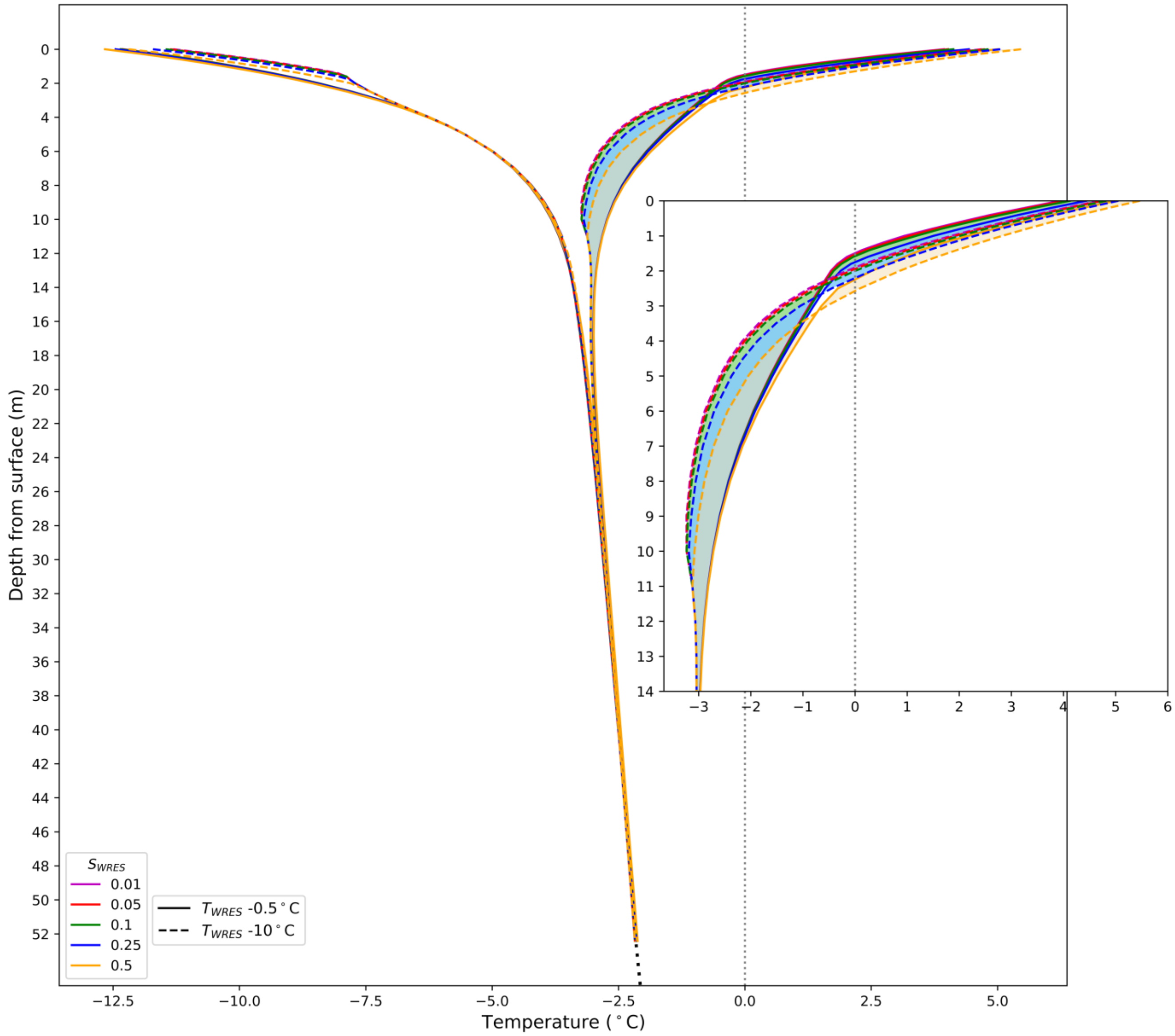

Figure 15. Ground temperature profiles for piecewise linear simulations using a high T_{WRES} value (solid lines) or low T_{WRES} value (dashed lines). 0°C is represented by a grey vertical dotted line. Zoomed-in inset shows maximum temperatures for upper 14 m of the model.

Figure 15 illustrates changes in the temperature profiles of piecewise linear simulations when decreasing T_{WRES} values from –0.5 °C to –10 °C. When T_{WRES} is kept constant at –0.5 °C, increasing the S_{WRES} value does not result in any significant change in the thermal profile. At a T_{WRES} of –10 °C, increasing the S_{WRES} value leads to thickening of the active layer.

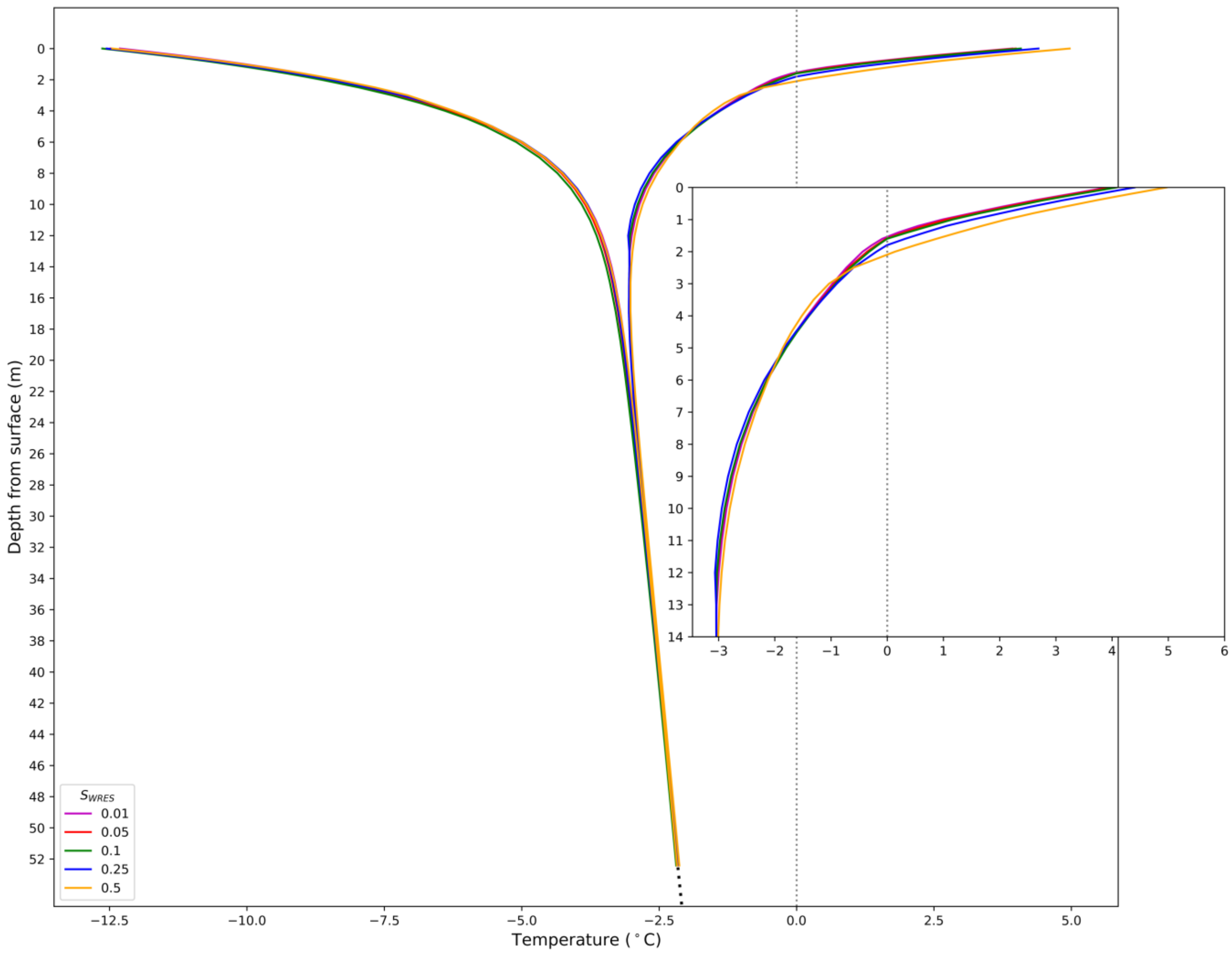

Figure 16. Ground temperature profiles for power law simulations. 0 °C is represented by a grey vertical dotted line. Zoomed-in inset shows maximum temperatures for upper 14 m of the model.

A similar pattern is seen in temperature profiles for the power law simulations (Figure 16), where models using higher S_{WRES} values have a deeper active layer. The difference in active layer depths between S_{WRES}= 0.01 and S_{WRES}= 0.5 is approximately 0.55 metres.

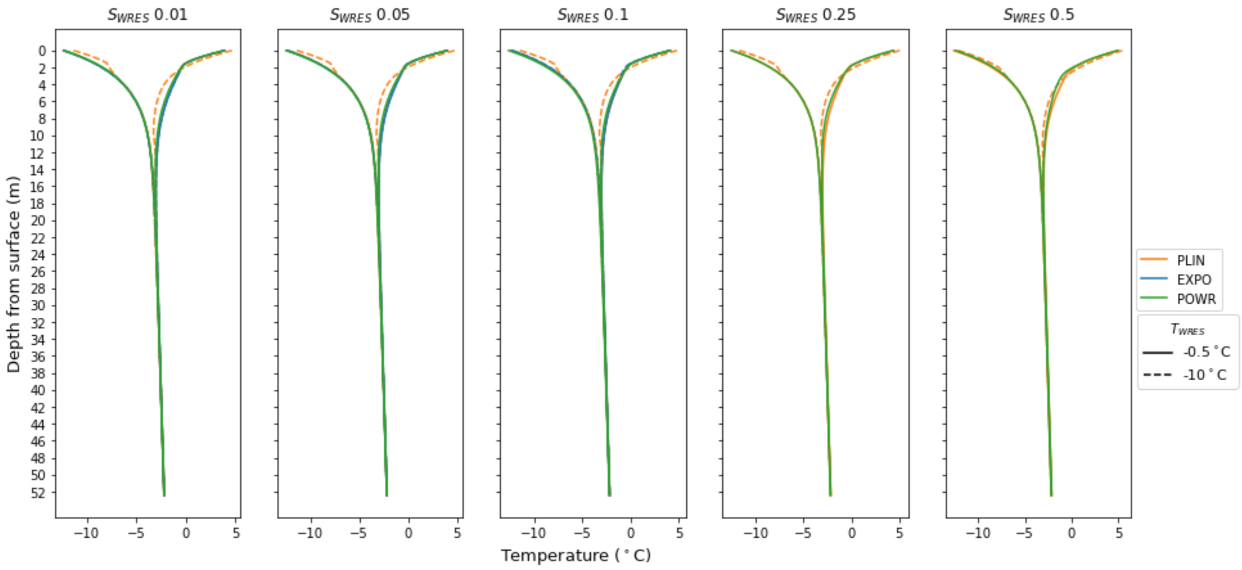

Figure 17. Temperature profiles for piecewise linear, exponential, and power law simulations. The solid line is T_{WRES} = –0.5 °C and dashed line is T_{WRES} = –10 °C. The temperature profiles for power law and exponential simulations are nearly identical (blue and green lines overlap).

Figure 17 compares ground temperature profiles for all three soil freezing functions with the same S_{WRES} values. For piecewise linear and exponential functions, the solid lines show models that use a T_{WRES} value of –0.5 °C whereas the dashed lines represent models where T_{WRES} = –10 °C is used. Thermal profiles using the power law freezing function are shown with solid lines (however these simulations do not have a T_{WRES} value). The solid lines in Figure 17 overlap, indicating that all three SFCCs have similar temperature envelopes even when changing the S_{WRES} value. The only temperature profiles that differ are those using a piecewise linear curve with T_{SWRES} of –10 °C (dashed orange line), as these models are completely unfrozen.

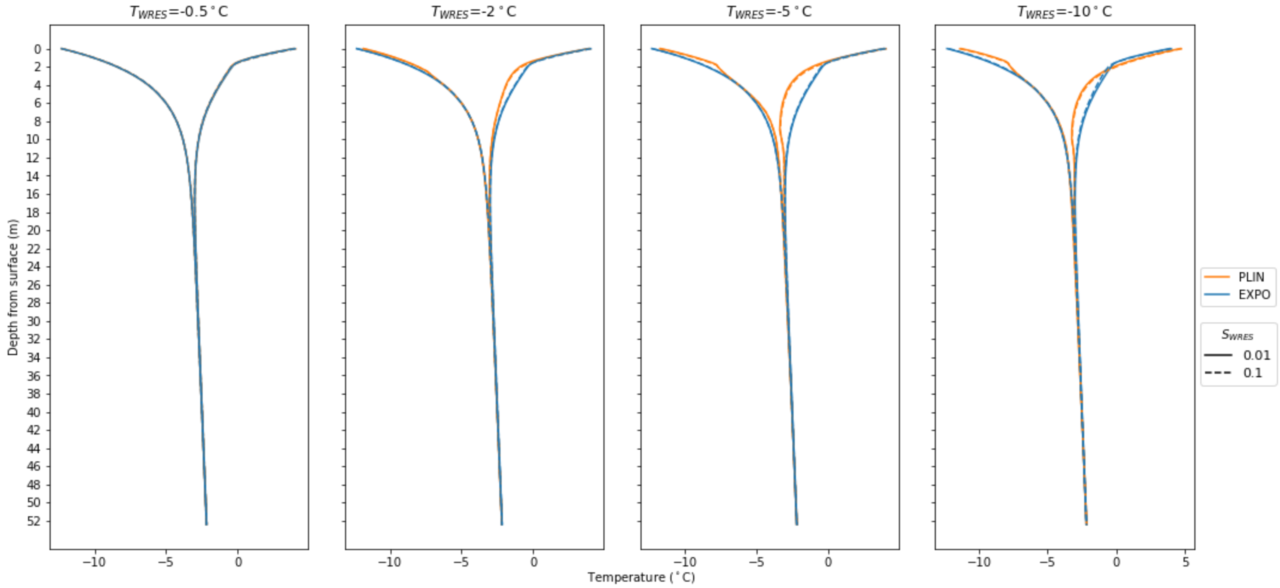

Figure 18. Temperature profiles for piecewise linear and exponential simulations. Solid line is S_{WRES} = 0.01 and dashed line is S_{WRES} = 0.1.

Figure 18 compares temperature profiles for piecewise linear and exponential with the same S_{WRES} and T_{WRES} value. The solid (S_{WRES}= 0.01) and dashed lines (S_{WRES} = 0.1) overlap, indicating that changing the S_{WRES} values does not change the temperature profiles for either piecewise linear or exponential SFCC's. However, there is a difference between piecewise linear and exponential when at lower T_{WRES} values; the change in slope in the piecewise linear profiles are due to wide slow phase changing regions (mushy zones) that are absent in the exponential SFCC models.

4.3 River discharge patterns

Depending on the soil freezing curve used, the freezing point depression may have a significant effect on the amount of groundwater discharged to the simulated river. The timing of stream discharge for all three soil freezing curve simulations follow the same pattern, where maximum spring freshet occurs 15 days after air temperature exceeds 0 °C (small peak at day 35 in Figures 19 and 20). The amount of stream discharge is similar for all power law simulations, piecewise linear simulations using T_{WRES} = –0.5 °C, and exponential simulations using T_{WRES} = –0.5 °C even when S_{WRES} value is increased (Figure 19a). With a low T_{WRES} value of –10 °C, there is significantly more stream discharge for piecewise linear simulations compared to the other two soil freezing curves (Figure 19*b*). Pore ice limits connectivity between the river and aquifer, thus the exponential and power law models that are more ice saturated have less groundwater discharge to the river. Higher S_{WRES} values lead to a less ice-saturated model, resulting in more groundwater connectivity and stream discharge. There is a significant amount of winter discharge to the stream, indicating increased baseflow and a different hydrologic regime.

Figure 20 compares the discharge for only the piecewise linear and exponential functions. Stream discharge is slightly greater with SWRES values of 0.1 (dashed lines) compared to SWRES values of 0.01 (solid lines) for both SFCCs. When comparing the effect of decreasing T_{WRES} on stream discharge, the exponential simulations stay constant while the piecewise linear simulations have significantly more discharge with lower T_{WRES} and continue to discharge water to the river even when air temperatures are below 0 °C as the model shifts from Scenario A and B to Scenario C (see Figure 21). These results suggest that differences in hydraulic connectivity between a piecewise linear and exponential SFCC is not significant if a high freezing point depression is used, however the type of SFCC is important with lower freezing point depression.

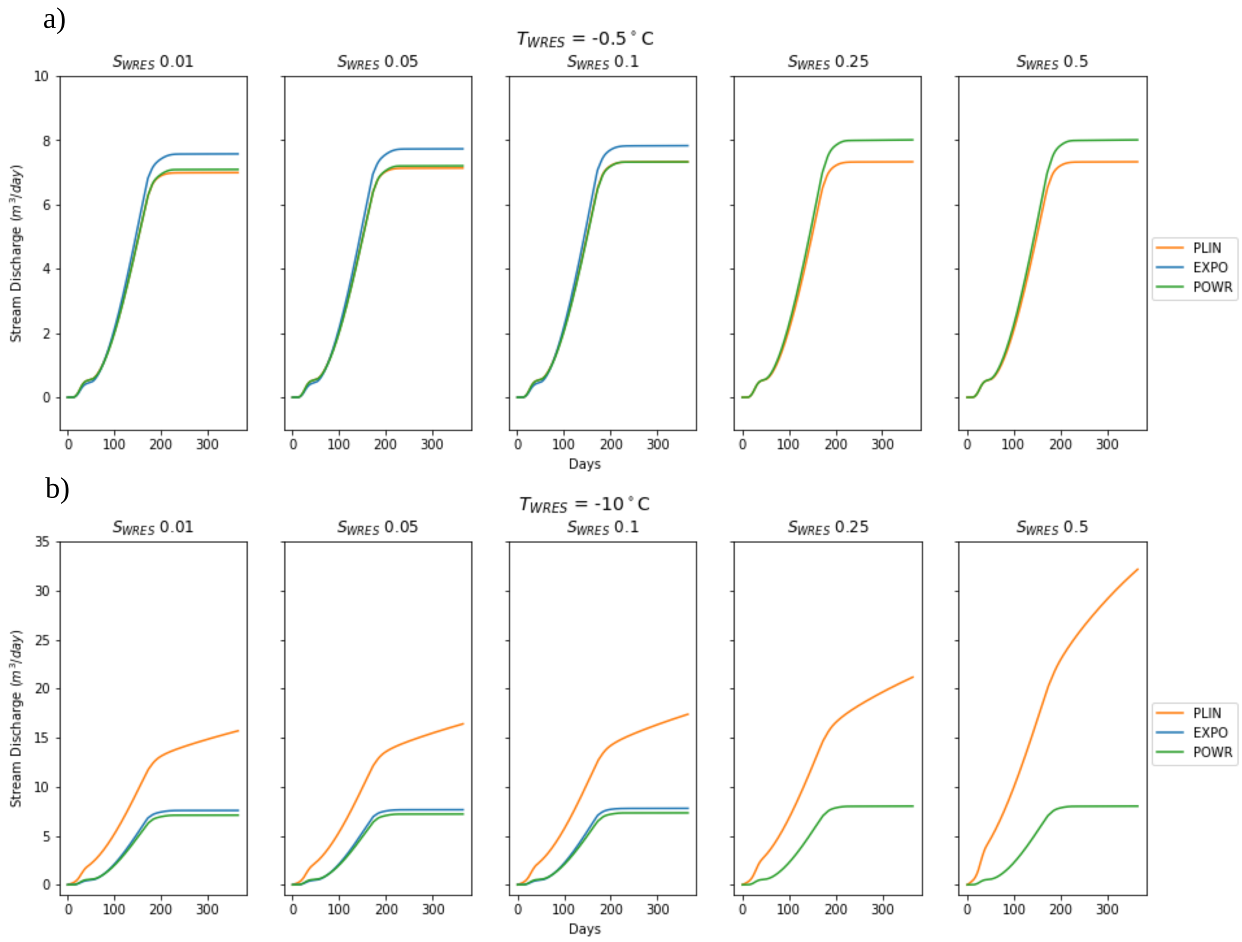

Figure 19. Annual cumulative stream discharge for piecewise linear SFCC ('PLIN', orange line), exponential SFCC ('EXPO', blue line), and power law SFCC ('POWR', green line) simulations using (a) T_{WRES} = –0.5 °C or (b) T_{WRES} = –10 °C. The blue lines representing exponential simulations are only shown in the first three plots as S_{WRES} 0.01, 0.05, and 0.1 were the only values tested for the exponential SFCC.

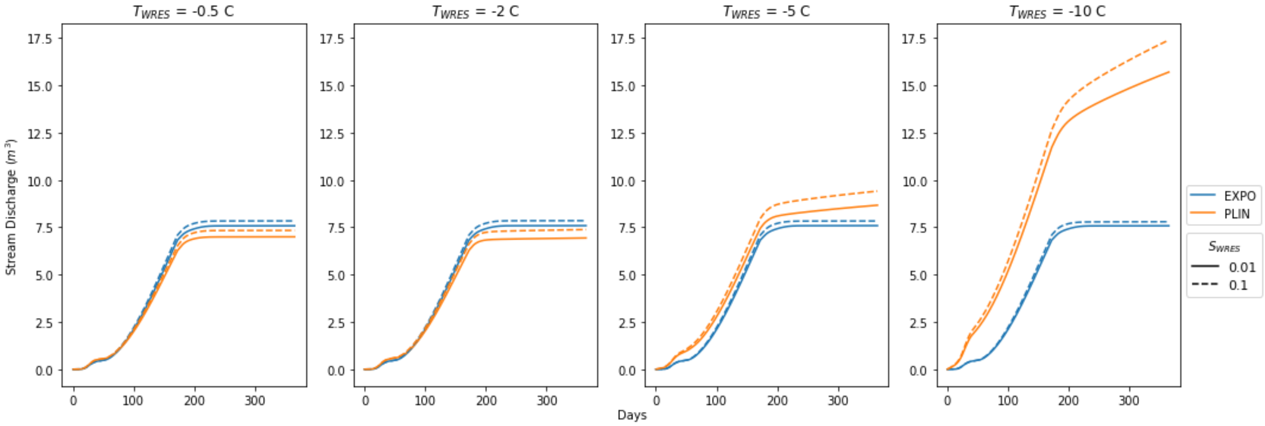

Figure 20. Annual cumulative stream discharge for piecewise linear SFCC simulations (‘PLIN’, orange line) and exponential SFCC simulations (‘EXPO’, blue line). Solid line is $S_{WRES} = 0.01$ and dashed line is $S_{WRES} = 0.1$.

4.4 Interpretation of hydrogeologic results

The type and parameterization of the SFCC has an important impact on the subsurface water storage and ice distribution of the model. Figure 21 conceptually illustrates the seasonal evolution of the active layer and groundwater flow pathways for different SFCC expressions and parameterizations. Each scenario (A, B, or C) represents a SFCC combination with S_{WRES} and T_{WRES} parameter values on extreme ends of the test value range (*i.e.*, Scenario A corresponds to lowest S_{WRES} and highest T_{WRES}, B: highest S_{WRES} and highest $T_{WRES,}$ C: lowest S_{WRES} and lowest T_{WRES}, and C: highest S_{WRES} and lowest T_{WRES}).

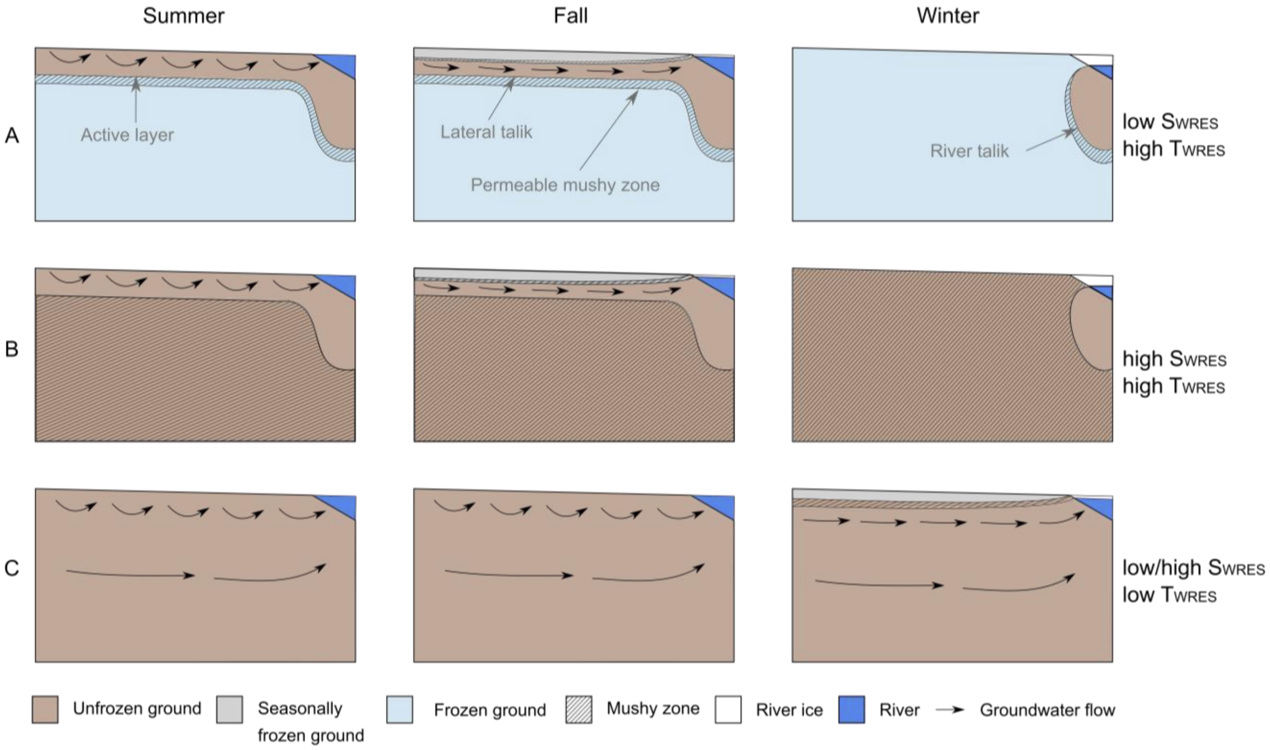

Figure 21. Conceptual model of shallow groundwater flow using different combinations of S_{WRES} and T_{WRES} values (A: low S_{WRES} and high T_{WRES}, B: high S_{WRES} and high T_{WRES}, C: low/high S_{WRES} and low T_{WRES}) for piecewise linear, exponential, and power law freezing functions.

In Scenario A, an active layer allows shallow groundwater flow in the summer, with a narrow mushy zone forming between the active layer and fully frozen permafrost. The mushy zone enables slow groundwater flow below the permafrost table. The active layer freezes from the top down in the fall (i.e., freezing front), opening to create a lateral talik between the active layer and permafrost table that acts as a conduit for groundwater flow. In the winter, a 20 m deep and 11 m wide isolated talik forms under the river. This scenario corresponds to a piecewise linear freezing function with low S_{WRES} (0.01) and high T_{WRES} (–0.5 °C), a power law freezing function with low S_{WRES} (0.01), or all exponential freezing function simulations. Scenario B is similar to A except that the ground doesn't fully freeze and form ice-rich permafrost at greater depths, instead forming a partially frozen zone with < 60% ice saturation. This scenario is seen with simulations using piecewise linear SFCC with high S_{WRES} (0.5) and high T_{WRES} (–0.5°C), or power law SFCC with high S_{WRES} (0.5).

In Scenario C, the model is completely unfrozen in the summer and only forms a shallow freezing layer in the winter. This allows for deep groundwater flow year-round, with only slightly less groundwater discharge to the river in the winter (vs in the summer) due to shallow seasonal freezing. Scenario C corresponds to a piecewise linear SFCC with low S_{WRES} (0.01) and low T_{WRES} (–10°C), or a piecewise linear SFCC with high S_{WRES} (0.5) and low T_{WRES} (–10°C). The degree of ice saturation in the winter freezing front increases with lower S_{WRES}. In this scenario, the discharge to the river is significantly greater due to the higher permeability and hydrologic connectivity of water-saturated soil, compared to the impermeable ice-rich soil in Scenario A and slow groundwater flow in Scenario B.

5. Conclusions

5.1 Limitations in modelling approach

While this research provides evidence of how different types and parameterizations of SFCCs may impact groundwater models, there are limitations in the current numerical model analysis. To make the model more tractable, the SFCCs used in this study do not include the hysteretic behaviour experimentally observed in some frozen soils (e.g., Koopmans & Miller, 1966; Pardo Lara, Berg, & Warland, 2020), which may change the properties of the porous medium depending on the history of freeze-thaw and unsaturation. Hu *et al.* (2020) argue that this hysteresis behaviour is significant when sub-freezing temperatures are close to 0°C and its effect on the content of unfrozen water should not be ignored.

To represent an archetypal permafrost landscape, the current model uses simple boundary conditions. However, some surface processes are ignored such as snowmelt, snow distribution, effect of vegetation, and seasonally variable albedo. These cold-region surface processes can significantly affect the ground thermal and hydrologic regime (Lamontagne-Hallé *et al*., 2020). Integrating a snowpack model may improve the timing and accuracy of snowmelt recharge and could provide insight on the regulatory effect of snowpack insulation on the extent of soil freezing.

5.2 Comparing literature values of SFCC parameters

Experimental methods allow researchers to determine the soil freezing point depression and residual unfrozen water content in many different types of permafrost soils. Using NMR and contact methods, Chuvilin *et al.* (2022) were able to obtain freezing points between –0.49 °C and –2.81 °C for sand, silt, and clay samples from the Yamal Peninsula permafrost. The minimum unfrozen water contents for these soil samples were found to be between 0.3 and 10 % by weight. They found that unfrozen water content was sensitive to the total organic carbon content, due to its high hydrophilicity and ability to hold water. Pardo Lara *et al*. (2020) found freezing point depression averages and standard deviations between –1.86 ± 0.05 °C and –2.1 ± 0.4 °C for sandy/clay loam samples collected in Ontario, Canada. Some soils show a much lower freezing point depression due to particle size distribution, clay content, and mineral composition. Roth and Boike (2001) found liquid water existing at a volume fraction of 0.05 as low as –15°C. Liu and Li (2012) determined soil-freezing characteristic curves using simple laboratory tests and found minimum unfrozen water content values of 6.12 wt % for silt samples (total water content between 22.7 and 23.6%) and 8.48 wt % for silty clay samples (total water content of about 22.94 %). The mean temperature at which minimum unfrozen water content occurred was found to be –4.0°C and –8.5°C for silt and silty clay, respectively. For clay with a total water content of about 35.5 %, the minimum unfrozen water content was approximately 12.65 % at –8 °C. Many studies also show that more liquid is retained for higher salinity soils (i.e., decreased freezing point depression) (e.g., Ming *et al*., 2020; Wang *et al*., 2018; Zhang *et al*., 2022). In summary, the measured freezing range of *in situ* and laboratory soil samples is highly variable and dependant on several chemical and mechanical properties of the soil such as solute concentration and pore size.

Previous modelling studies use S_{WRES} values ranging between 0 and 0.05 and T_{WRES} values between –0.0005 °C and –2 °C for piecewise linear SFCC (Grenier *et al*., 2013; Jame, 1977; Lamontagne-Hallé *et al*., 2018; McKenzie *et al*., 2007; Scheidegger, 2016). For exponential SFCC, S_{WRES} values between 0.05 and 0.5 and *w* parameters between 0.005 and 0.5 have been used in permafrost models (Lyon, 2019; McKenzie *et al*., 2007). Parameterizations for the power law SFCC have been experimentally determined by researchers such as Ren *et al.*, (2017), who have found alpha and beta values ranging between 0.018 and 0.212 and –0.152 and –0.584, respectively. This thesis demonstrates how the type and parameterization of SFCC influences model behaviour and outcomes, however, many of the models listed above implement a wide range of parameter values that may not be quantitatively supported. There are many different types of soil in nature, and not all empirical relationships that describe soil freezing can be applied to all types of soil. It is important to consider the characterization of soil, permafrost regime (i.e., discontinuous, continuous, degrading, and/or stable), and degree of saturation intended to be modelled when defining the SFCC parameters. The appropriate choice of SFCC curve can significantly improve the efficiency and accuracy of numerical models with soil freezing.

5.3 Choosing a SFCC and its parameterization

There is no uniform procedure or standard method when choosing a soil freezing characteristic curve in numerical groundwater models. Some modelers employ an empirical SFCC that relies on a predefined function where the parameters are estimated from laboratory measurements. These include piecewise linear, power law, and exponential functions analysed in this study. Other scholars use a mechanistic approach, which consists of SFCCs derived from SWCCs via a form of the Clapeyron equation (e.g. Brooks and Corey (1964), van Genuchten (1980), and Fredlund and Xing (1994)). When choosing the type and parameterization of SFCC, it is important to consider the study objectives, including the spatial and temporal scale of the study, as well as the limitations of the model code and availability of measured data. For site-specific models, SFCC parameters should be calibrated based on field or laboratory data. Reliable measurement of the SFCC depends on the accurate determination of sub-zero temperatures and unfrozen water content, or pore water suction and moisture content for SWCCs. While this may be difficult due to experimental limitations associated with resolution and precision requirements, interpolated field data can be derived from point measurements to generate the SFCC or SWCC. SFCC selection may also be based on known soil characteristics, such as soil porosity, texture, composition, degree of saturation, presence of dissolved solids, etc., which can be site-specific and time varying (Devoie *et al.*, 2022). However, it can be expensive and logistically difficult to collect such a dataset in an arctic environment, and interpolating sporadic data may result in uncertainties and misrepresentation (Lamontagne-Hallé *et al.*, 2020). Although there are various quantitative methods to evaluate the accuracy of calibration of a groundwater model (Anderson & Woessner, 1992; Reilly & Harbaugh, 2004), it is more important to consider the study objectives and appropriateness of the conceptual system (e.g., do the SFCC parameters have clear physical meanings and are the values reasonable?) rather than obtaining the smallest differences between simulated values and real-world measurements. The choice and parameterization of SFCC can be validated by the ability of the groundwater model to reproduce past behaviour of a reference system, or by comparison against benchmark models.

For hypothetical or conceptual models that are not data rich, the choice of SFCC and estimation of SFCC parameters depends on the modelling scenario and the type of landscape. Hypothetical models are not calibrated, but input data such as SFCC parameters should be adjusted during model development to ensure the model matches the idealized system. The type and parameterization of SFCC can be estimated from existing models or from sites with similar soil types and frost regimes. For example, using a piecewise linear SFCC with low S_{WRES} and high T_{WRES} may be suitable for modelling a landscape with deep and stable permafrost that is completely ice saturated in winter (e.g., Carpino *et al.*, 2021). However, using a piecewise linear SFCC with high S_{WRES} and high T_{WRES} is more representative of ground that is water saturated even in winter and has a shallow seasonal freezing front (e.g., Osterkamp, 2005). A degrading permafrost system, such as thin discontinuous permafrost responding to ground surface warming, may be better represented by a piecewise linear with low T_{WRES}. Ren *et al*. (2017) found that exponential and van Genuchten equations are more suitable for sandy soils, whereas the power relationship could reasonably fit SFCC for soils with different particle sizes, excluding saline silt.

5.4 Summary of findings

This thesis uses two-dimensional numerical modelling to investigate how various parameterizations of three widely used soil-freezing curves affect cryohydrogeological model results such as permafrost formation and persistence, soil temperature, and stream discharge. Understanding groundwater and heat flow processes in permafrost environments is becoming increasingly important as climate change continues to impact northern hydrological regimes. Numerical modelling of cold regions allows researchers to evaluate and predict the future state of groundwater flow systems, however, appropriate parameterization is required for accurate simulation of dynamic freeze-thaw processes.

The model results suggest that the type and parameterization of SFCC used leads to significant differences in the ice saturation of permafrost and hydrological connectivity. For simulations using a piecewise linear or power law freezing function, changing the freezing point depression will significantly affect the existence of ice-rich permafrost, the depth of seasonal thaw, and the thickness of the active layer. However, the freezing point depression is not significant when using an exponential freezing function; the degree of ice saturation, the thickness of the active layer, and stream discharge is the same for all tested T_{WRES} values. The difference in model outcomes for the three types of SFCC is only notable when a low freezing point depression (low T_{WRES} value) is used. Thus, the choice of appropriate SFCC is made easier if a narrow freezing range (high T_{WRES} value) is specified. This often leads to numeric instabilities in models.

Additionally, the results illustrate that the residual unfrozen water content (S_{WRES} value) also has a large influence on thermal regimes and ice/water saturation. Researchers developing numerical models may increase the S_{WRES} value when trying to limit computation time and model complexity, however, this may introduce a significant source of error. For example, the ground temperature profile shows increasing S_{WRES} from 0.01 to 0.5 for the piecewise linear function (Figure 15) will lead to thickening of the active layer by 0.7 metres. This difference can be substantial for models with only a few metres of seasonal thawing or for small, metre-scale models. It is important to balance ease of modelling and model complexity with a S_{WRSE} value that is physically realistic.

My results show that changing the T_{WRES} value has a larger impact on permafrost formation and thaw than changing the S_{WRES} value for piecewise linear and power law SFCC. This is because increasing the T_{WRES} value from -10 °C to –0.5 °C increases the slope of the soil-freezing function more than increasing the S_{WRES} value from 0.01 to 0.5. Using a steeper freezing function results in a narrower freezing front and mushy zone. The shape of the freezing function controls the rate of latent heat release. Differences in the rate and depth of the freezing front between high and low T_{WRES} simulations may be due to the large amount of latent heat released for lower T_{WRES}, which hinders additional ice formation and creates a steeper temperature divide between the fully frozen and unfrozen regions. Because the effect of latent heat largely controls the distribution of temperature and ice, the shape of the soil-freezing function governs the hydrological regime of permafrost models.

The parameterization of SFCCs in numerical modelling is highly important and choosing an inappropriate parameter can lead to misrepresentation of the hydrological and thermodynamic system.

While there is no universal procedure for choosing a SFCC, different approaches are more suitable for different modelling scenarios (e.g., site specific versus conceptual models). Factors such as soil type, annual temperature variations, and permafrost regime should be considered when parameterizing the soil freezing function. For site specific models, the relationship between unfrozen water content and temperature can be determined experimentally, however, the mechanical and chemical properties of soils vary greatly with soil type, so it is difficult to generalize the empirical formula from one soil to another (Bai *et al*., 2018; Devoie *et al*., 2022). For sites that are data rich, the model can be calibrated by fitting model results to field or experimental data. The closeness of fit between simulated and observed values is only one aspect of model calibration. It is also important to consider the conceptualization of the system and appropriateness of the model to address problem objectives. When evaluating the adequacy of a SFCC, the input parameters, model output, and appropriate mathematical representation of soil-specific processes should be evaluated to ensure they all represent the same analysis. This is especially important for hypothetical or conceptual models. The model used in this thesis is one of an idealized or representative system (simple permafrost landscape where groundwater discharges into a downgradient river) as opposed to a model of a specific system. Input parameters were adjusted to evaluate how the model responds to various SFCC parameterizations. The relative effect of the type and parameterization of SFCC may differ under different modelling scenarios or settings. For example, changing the initial saturation, boundary temperature conditions, or water input rate of the model may change model outputs such as stream discharge and ice saturation even with the same SFCC parameterization. Sensitivity analysis is therefore an important component of model calibration and evaluation for cryohydrogeological modelling.

7. References

Andersland, O. B., & Ladanyi, B. (1994). Physical and Thermal Properties. In O. B. Andersland & B. Ladanyi (Eds.), *An Introduction to Frozen Ground Engineering* (pp. 23–63). Springer US. https://doi.org/10.1007/978-1-4757-2290-1_2

Anderson, D. M., & Morgenstern, N. R. (1973). *Permafrost: North American Contribution [to The] Second International Conference*. National Academies.

Anderson, D. M., & Tice, A. R. (1972). Predicting unfrozen water contents in frozen soils from surface area measurements. *Highway Research Record*, *393*(2), 12–18.

Anderson, M. P., & Woessner, W. W. (1992). *Applied Groundwater Modeling: Simulation of Flow and Advective Transport*. Elsevier Science.

Azmatch, T. F., Sego, D. C., Arenson, L. U., & Biggar, K. W. (2012a). Using soil freezing characteristic curve to estimate the hydraulic conductivity function of partially frozen soils. *Cold Regions Science and Technology, 83–84*, 103–109. https://doi.org/10.1016/j.coldregions.2012.07.002

Azmatch, T.F, Sego, D., Arenson, L.U, & Biggar, K.W (2012b). New ice lens initiation condition for frost heave in fine-grained soils. *Cold Regions Science and Technology, 82,* 8–13. https://doi.org/10.1016/j.coldregions.2012.05.003

Bai, R., Lai, Y., Zhang, M., & Yu, F. (2018). Theory and application of a novel soil freezing characteristic curve. *Applied Thermal Engineering, 129*, 1106–1114. https://doi.org/10.1016/j.applthermaleng.2017.10.121

Ballinger, T. J., Overland, J. E., Wang, M., Bhatt, U. S., Hanna, E., Hanssen-Bauer, I., Kim, S.-J., Thoman, R. L., & Walsh, J. E. (2020). *Arctic Report Card 2020: Surface Air Temperature*. https://doi.org/10.25923/GCW8-2Z06

Bense, V. F., Kooi, H., Ferguson, G., & Read, T. (2012). Permafrost degradation as a control on hydrogeological regime shifts in a warming climate. *Journal of Geophysical Research: Earth Surface*, *117*(F3). https://doi.org/10.1029/2011JF002143

Blanchard, D., & Fremond, M. (1985). *Soils frost heaving and thaw settlement*. Rotterdam, A.A. Balkema. Netherlands. P.

Brooks, R. H., & Corey, A. (1964). *Hydraulic Properties of Porous Media and Their Relation to Drainage Design*. https://doi.org/10.13031/2013.40684

Cahn, J. W., Dash, J. G., & Fu, H. (1992). Theory of ice premelting in monosized powders. *Journal of Crystal Growth*, *123*(1), 101–108. https://doi.org/10.1016/0022-0248(92)90014-A

Carpino, O., Haynes, K., Connon, R., Craig, J., Devoie, É., & Quinton, W. (2021). Long-term climate-influenced land cover change in discontinuous permafrost peatland complexes. *Hydrology and Earth System Sciences*, *25*(6), 3301–3317. https://doi.org/10.5194/hess-25-3301-2021

Chai, M., Zhang, J., Hu, Z., Mu, Y., Sun, G., & Yin, Z. (2018). A method for calculating unfrozen water content of silty clay with consideration of freezing point. *Applied Clay Science*, *161*, 474–481. https://doi.org/10.1016/j.clay.2018.05.015

Chen, L., Liang, J., Qin, S., Liu, L., Fang, K., Xu, Y., Ding, J., Li, F., Luo, Y., & Yang, Y. (2016). Determinants of carbon release from the active layer and permafrost deposits on the Tibetan Plateau. *Nature Communications*, *7*(1), 13046. https://doi.org/10.1038/ncomms13046

Chuvilin, E. M., Bukhanov, B. A., Mukhametdinova, A. Z., Grechishcheva, E. S., Sokolova, N. S., Alekseev, A. G., & Istomin, V. A. (2022). Freezing point and unfrozen water contents of permafrost soils: Estimation by the water potential method. *Cold Regions Science and Technology*, *196*, 103488. https://doi.org/10.1016/j.coldregions.2022.103488

Connon, R. F., Quinton, W. L., Craig, J. R., & Hayashi, M. (2014). Changing hydrologic connectivity due to permafrost thaw in the lower Liard River valley, NWT, Canada. *Hydrological Processes*, *28*(14), 4163–4178. https://doi.org/10.1002/hyp.10206

Dall'Amico, M. (2010). *Coupled Water and Heat Transfer in Permafrost Modeling* [Phd, University of Trento]. http://eprints-phd.biblio.unitn.it/335/

Dash, J. G., Fu, H., & Wettlaufer, J. S. (1995). The premelting of ice and its environmental consequences. *Reports on Progress in Physics*, *58*(1), 115–167. https://doi.org/10.1088/0034-4885/58/1/003

de Grandpré, I., Fortier, D., & Stephani, E. (2012). Degradation of permafrost beneath a road embankment enhanced by heat advected in groundwater. *Canadian Journal of Earth Sciences*, *49*(8), 953–962. https://doi.org/10.1139/e2012-018

Devoie, É. (2020). *The changing influence of permafrost on peatlands hydrology* [Doctoral Thesis]. University of Waterloo.

Devoie, É., & Craig, J. (2020). A Semi-Analytical Interface Model of Soil Freeze/Thaw and Permafrost Evolution. *Water Resources Research*, *56*. https://doi.org/10.1029/2020WR027638

Devoie, É. G., Gruber, S., & McKenzie, J. M. (2022). A Repository of 100+ Years of Measured Soil Freezing Characteristic Curves. *Earth System Science Data Discussions*, 1–21. https://doi.org/10.5194/essd-2022-61

Durner, W. (1994). Hydraulic conductivity estimation for soils with heterogeneous pore structure. *Water Resources Research*, *30*(2), 211–223. https://doi.org/10.1029/93WR02676

Evans, S. G., & Ge, S. (2017). Contrasting hydrogeologic responses to warming in permafrost and seasonally frozen ground hillslopes. *Geophysical Research Letters*, *44*(4), 1803–1813. https://doi.org/10.1002/2016GL072009

Flerchinger, G. N., Seyfried, M. S., & Hardegree, S. P. (2006). Using Soil Freezing Characteristics to Model Multi-Season Soil Water Dynamics. *Vadose Zone Journal*, *5*(4), 1143–1153. https://doi.org/10.2136/vzj2006.0025

Fredlund, D. G., & Xing, A. (1994). Equations for the soil-water characteristic curve. *Canadian Geotechnical Journal*, *31*(4), 521–532. https://doi.org/10.1139/t94-061

Fredlund, D. G., Xing, A., & Huang, S. (1994). Predicting the permeability function for unsaturated soils using the soil-water characteristic curve. *Canadian Geotechnical Journal*, *31*(4), 533–546. https://doi.org/10.1139/t94-062

Ge, S., McKenzie, J., Voss, C., & Wu, Q. (2011). Exchange of groundwater and surface-water mediated by permafrost response to seasonal and long term air temperature variation. *Geophysical Research Letters*, *38*(14). https://doi.org/10.1029/2011GL047911

Grenier, C., Anbergen, H., Bense, V., Chanzy, Q., Coon, E. T., Collier, N. O., Costard, F., Ferry, M., Frampton, A., Frederick, J., Gonçalvès, J., Holmén, J., Jost, A., Kokh, S., Kurylyk, B., McKenzie, J., Molson, J., Mouche, E., Orgogozo, L., … Voss, C. (2018). Groundwater flow and heat transport for systems undergoing freeze-thaw: Intercomparison of numerical simulators for 2D test cases. *Advances in Water Resources*, *114*(C), Article SAND-2018-1705J. https://doi.org/10.1016/j.advwatres.2018.02.001

Grenier, C., Régnier, D., Mouche, E., Benabderrahmane, H., Costard, F., & Davy, P. (2013). Impact of permafrost development on groundwater flow patterns: A numerical study considering freezing cycles on a two-dimensional vertical cut through a generic river-plain system. *Hydrogeology Journal*, *21*(1), 257–270. https://doi.org/10.1007/s10040-012-0909-4

Gruber, S. (2012). Derivation and analysis of a high-resolution estimate of global permafrost zonation. *The Cryosphere*, *6*(1), 221–233. https://doi.org/10.5194/tc-6-221-2012

Hansson, K., Simunek, J., Jirka, Mizoguchi, M., Lundin, L.-C., & Van Genuchten, M. (2004). Water Flow and Heat Transport in Frozen Soil. *Vadose Zone Journal - VADOSE ZONE J*, *3*, 527–533. https://doi.org/10.2136/vzj2004.0693

Hu, G., Zhao, L., Zhu, X., Wu, X., Wu, T., Li, R., Xie, C., & Hao, J. (2020). Review of algorithms and parameterizations to determine unfrozen water content in frozen soil. *Geoderma*, *368*, 114277. https://doi.org/10.1016/j.geoderma.2020.114277

Jame, Y.-W. (1977). *Heat and mass transfer in freezing unsaturated soil*. https://harvest.usask.ca/handle/10388/etd-11282008-091133

Jame, Y.-W., & Norum, D. I. (1980). Heat and mass transfer in a freezing unsaturated porous medium. *Water Resources Research*, *16*(4), 811–819. https://doi.org/10.1029/WR016i004p00811

Jin, X., Yang, W., Gao, X., Zhao, J.-Q., Li, Z., & Jiang, J. (2020). Modeling the Unfrozen Water Content of Frozen Soil Based on the Absorption Effects of Clay Surfaces. *Water Resources Research*, *56*(12), e2020WR027482. https://doi.org/10.1029/2020WR027482

Koopmans, R. W. R., & Miller, R. D. (1966). Soil Freezing and Soil Water Characteristic Curves. *Soil Science Society of America Journal*, *30*(6), 680–685. https://doi.org/10.2136/sssaj1966.03615995003000060011x

Kozlowski, T. (2003). A comprehensive method of determining the soil unfrozen water curves: 1. Application of the term of convolution. *Cold Regions Science and Technology*, *36*(1), 71–79. https://doi.org/10.1016/S0165-232X(03)00007-7

Kozlowski, T. (2004). Soil freezing point as obtained on melting. *Cold Regions Science and Technology*, *38*(2), 93–101. https://doi.org/10.1016/j.coldregions.2003.09.001

Kozlowski, T. (2007). A semi-empirical model for phase composition of water in clay–water systems. *Cold Regions Science and Technology*, *49*(3), 226–236. https://doi.org/10.1016/j.coldregions.2007.03.013

Kozlowski, T., & Nartowska, E. (2013). Unfrozen Water Content in Representative Bentonites of Different Origin Subjected to Cyclic Freezing and Thawing. *Vadose Zone Journal*, *12*(1), vzj2012.0057. https://doi.org/10.2136/vzj2012.0057

Kurylyk, B. L., & Walvoord, M. A. (2021). Permafrost Hydrogeology. In D. Yang & D. L. Kane (Eds.), *Arctic Hydrology, Permafrost and Ecosystems* (pp. 493–523). Springer International Publishing. https://doi.org/10.1007/978-3-030-50930-9_17

Kurylyk, B. L., & Watanabe, K. (2013). The mathematical representation of freezing and thawing processes in variably-saturated, non-deformable soils. *Advances in Water Resources*, *60*, 160–177. https://doi.org/10.1016/j.advwatres.2013.07.016

Lamontagne-Hallé, P., McKenzie, J. M., Kurylyk, B. L., Molson, J., & Lyon, L. N. (2020). Guidelines for cold-regions groundwater numerical modeling. *WIREs Water*, *7*(6), e1467. https://doi.org/10.1002/wat2.1467

Lamontagne-Hallé, P., McKenzie, J. M., Kurylyk, B. L., & Zipper, S. C. (2018). Changing groundwater discharge dynamics in permafrost regions. *Environmental Research Letters*, *13*(8), 084017. https://doi.org/10.1088/1748-9326/aad404

Lamontagne-Hallé1, P., McKenzie1, J. M., Kurylyk, B. L., Zipper, S. C., & Fortier, D. (in preparation). *Role of surface boundary conditions and groundwater flow for permafrost thaw estimates and groundwater discharge patterns*.

Li, Q., Sun, S., & Xue, Y. (2010). Analyses and development of a hierarchy of frozen soil models for cold region study. *Journal of Geophysical Research: Atmospheres*, *115*(D3). https://doi.org/10.1029/2009JD012530

Li, R., Zhao, L., Wu, T., Wang, Q., Ding, Y., Yao, J., Wu, X., Hu, G., Xiao, Y., Du, Y., Zhu, X., Qin, Y., Yang, S., Bai, R., Du, E., Liu, G., Zou, D., Qiao, Y., & Shi, J. (2019). Soil thermal conductivity and its influencing factors at the Tanggula permafrost region on the Qinghai–Tibet Plateau. *Agricultural and Forest Meteorology*, *264*, 235–246. https://doi.org/10.1016/j.agrformet.2018.10.011

Li, S., Wang, C., Shi, L., & Yin, N. (2019). Statistical characteristics of the thermal conductivity of frozen clay at different water contents. *Results in Physics*, *13*, 102179. https://doi.org/10.1016/j.rinp.2019.102179

Liu, B., & Li, D. (2012). A simple test method to measure unfrozen water content in clay–water systems. *Cold Regions Science and Technology*, *78*, 97–106. https://doi.org/10.1016/j.coldregions.2012.02.001

Lunardini, V. J. (1988). Freezing soil with an unfrozen water content and variable thermal properties. *This Digital Resource Was Created from Scans of the Print Resource*. https://erdc-library.erdc.dren.mil/jspui/handle/11681/9076

Lundin, L.-C. (1990). Hydraulic properties in an operational model of frozen soil. *Journal of Hydrology*, *118*(1), 289–310. https://doi.org/10.1016/0022-1694(90)90264-X

Lyon, L. (2019). *Does sporadic permafrost influence catchment-scale groundwater processes?* [Masters thesis]. McGill University.

Ma, T., Wei, C., Xia, X., Zhou, J., & Chen, P. (2017). Soil Freezing and Soil Water Retention Characteristics: Connection and Solute Effects. *Journal of Performance of Constructed Facilities*, *31*(1), D4015001. https://doi.org/10.1061/(ASCE)CF.1943-5509.0000851

McKenzie, J. M., & Voss, C. I. (2013). Permafrost thaw in a nested groundwater-flow system. *Hydrogeology Journal*, *21*(1), 299–316. https://doi.org/10.1007/s10040-012-0942-3

McKenzie, J. M., Voss, C. I., & Siegel, D. I. (2007). Groundwater flow with energy transport and water–ice phase change: Numerical simulations, benchmarks, and application to freezing in peat bogs. *Advances in Water Resources*, *30*(4), 966–983. https://doi.org/10.1016/j.advwatres.2006.08.008

Ming, F., Chen, L., Li, D., & Du, C. (2020). Investigation into Freezing Point Depression in Soil Caused by NaCl Solution. *Water*, *12*, 2232. https://doi.org/10.3390/w12082232

Mottaghy, D., & Rath, V. (2006). Latent heat effects in subsurface heat transport modeling and their impact on paleotemperature reconstructions. *Geophysical Journal International*, *164*, 236–245. https://doi.org/10.1111/j.1365-246X.2005.02843.x

Osterkamp, T. E. (2005). The recent warming of permafrost in Alaska. *Global and Planetary Change*, *49*(3), 187–202. https://doi.org/10.1016/j.gloplacha.2005.09.001

Painter, S. L., & Karra, S. (2014). Constitutive Model for Unfrozen Water Content in Subfreezing Unsaturated Soils. *Vadose Zone Journal*, *13*(4), vzj2013.04.0071. https://doi.org/10.2136/vzj2013.04.0071

Pardo Lara, R., Berg, A., & Warland, J. (2020). *Implications of measurement metrics on soil freezing curves: A simulation of freeze-thaw hysteresis*. https://doi.org/10.22541/au.160466100.02966301/v1

Pardo Lara, R., Berg, A., Warland, J., & Tetlock, E. (2020). In Situ Estimates of Freezing/Melting Point Depression in Agricultural Soils Using Permittivity and Temperature Measurements. *Water Resources Research*, *56*, e2019WR026020. https://doi.org/10.1029/2019WR026020

Pepin, N., Bradley, R. S., Diaz, H. F., Baraer, M., Caceres, E. B., Forsythe, N., Fowler, H., Greenwood, G., Hashmi, M. Z., Liu, X. D., Miller, J. R., Ning, L., Ohmura, A., Palazzi, E., Rangwala, I., Schöner, W., Severskiy, I., Shahgedanova, M., Wang, M. B., … Mountain Research Initiative EDW Working Group. (2015). Elevation-dependent warming in mountain regions of the world. *Nature Climate Change*, *5*(5), 424–430. https://doi.org/10.1038/nclimate2563

Qiu, E., Wan, X., Qu, M., Zheng, L., Zhong, C., Gong, F., & Liu, L. (2020). Estimating Unfrozen Water Content in Frozen Soils Based on Soil Particle Distribution. *Journal of Cold Regions Engineering*, *34*(2), 04020002. https://doi.org/10.1061/(ASCE)CR.1943-5495.0000208

Reilly, T., & Harbaugh, A. (2004). *Guidelines for Evaluating Ground-Water Flow Models*.

Ren, J., Vanapalli, S., & Han, Z. (2017). Soil freezing process and different expressions for the soil-freezing characteristic curve. *Sciences in Cold and Arid Regions*, *9*, 221–228. https://doi.org/10.3724/SP.J.1226.2017.00221

Ren, J., & Vanapalli, S. K. (2019). Comparison of Soil-Freezing and Soil-Water Characteristic Curves of Two Canadian Soils. *Vadose Zone Journal*, *18*(1), 180185. https://doi.org/10.2136/vzj2018.10.0185

Romanovsky, V., Burgess, M., Smith, S., Yoshikawa, K., & Brown, J. (2002). Permafrost temperature records: Indicators of climate change. *Eos, Transactions American Geophysical Union*, *83*(50), 589–594. https://doi.org/10.1029/2002EO000402

Romanovsky, V. E., Smith, S. L., & Christiansen, H. H. (2010). Permafrost thermal state in the polar Northern Hemisphere during the international polar year 2007–2009: A synthesis. *Permafrost and Periglacial Processes*, *21*(2), 106–116. https://doi.org/10.1002/ppp.689

Romanovsky, V., & Osterkamp, T. (2000). Effects of unfrozen water on heat and mass transport in the active layer and permafrost. *Permafrost and Periglacial Processes - PERMAFROST PERIGLACIAL PRO*, *11*, 219–239. https://doi.org/10.1002/1099-1530(200007/09)11:33.0.CO;2-7

Roth, K., & Boike, J. (2001). Quantifying the thermal dynamics of a permafrost site near Ny-Ålesund, Svalbard. *Water Resources Research*, *37*(12), 2901–2914. https://doi.org/10.1029/2000WR000163

Rühaak, W., Anbergen, H., Grenier, C., McKenzie, J., Kurylyk, B. L., Molson, J., Roux, N., & Sass, I. (2015). Benchmarking Numerical Freeze/Thaw Models. *Energy Procedia*, *76*, 301–310. https://doi.org/10.1016/j.egypro.2015.07.866

Scheidegger, J. (2016). Coupled modelling of permafrost and groundwater: A case study approach. *British Geological Survey*. https://www.semanticscholar.org/paper/Coupled-modelling-of-permafrost-and-groundwater-%3A-a-Scheidegger/63367fcb74335139405c6238219bcf3e0ae4bfb8

Serreze, M. C., Walsh, J. E., Chapin, F. S., Osterkamp, T., Dyurgerov, M., Romanovsky, V., Oechel, W. C., Morison, J., Zhang, T., & Barry, R. G. (2000). Observational Evidence of Recent Change in the Northern High-Latitude Environment. *Climatic Change*, *46*(1), 159–207. https://doi.org/10.1023/A:1005504031923

Sheshukov, A. Y., & Nieber, J. L. (2011). One-dimensional freezing of nonheaving unsaturated soils: Model formulation and similarity solution. *Water Resources Research*, *47*(11). https://doi.org/10.1029/2011WR010512

Sjöberg, Y., Coon, E., K. Sannel, A. B., Pannetier, R., Harp, D., Frampton, A., Painter, S. L., & Lyon, S. W. (2016). Thermal effects of groundwater flow through subarctic fens: A case study based on field observations and numerical modeling. *Water Resources Research*, *52*(3), 1591–1606. https://doi.org/10.1002/2015WR017571

Stephani, E., Fortier, D., Shur, Y., Fortier, R., & Doré, G. (2014). A geosystems approach to permafrost investigations for engineering applications, an example from a road stabilization experiment, Beaver Creek, Yukon, Canada. *Cold Regions Science and Technology*, *100*, 20–35. https://doi.org/10.1016/j.coldregions.2013.12.006

Tice, A. R., Anderson, D. M., & Banin, A. (1976). *The Prediction of Unfrozen Water Contents in Frozen Soils from Liquid Limit Determinations*. Department of Defense, Army, Corps of Engineers, Cold Regions Research and Engineering Laboratory.

Tuladhar, R., Marshall, A., & Sivakugan, N. (2020). 10—Use of recycled concrete aggregate for pavement construction. In F. Pacheco-Torgal, Y. Ding, F. Colangelo, R. Tuladhar, & A. Koutamanis (Eds.), *Advances in Construction and Demolition Waste Recycling* (pp. 181–197). Woodhead Publishing. https://doi.org/10.1016/B978-0-12-819055-5.00010-3

van Genuchten, M. Th. (1980). A Closed-form Equation for Predicting the Hydraulic Conductivity of Unsaturated Soils. *Soil Science Society of America Journal*, *44*(5), 892–898. https://doi.org/10.2136/sssaj1980.03615995004400050002x

Voss, C. I., & Provost, A. M. (2010). *SUTRA A Model for Saturated-Unsaturated, Variable-Density Ground-Water Flow with Solute or Energy Transport* (No. 02–4231; Water-Resources Investigations Report). U.S Geological Survey.

Voss, C. I., Provost, A. M., McKenzie, J. M., & Kurylyk, B. L. (2017). *SUTRA, a Model for Saturated Unsaturated, Variable Density Groundwater Flow with Solute or Energy Transport Documentation of the Freeze Thaw Capability, Saturation and Relative Permeability Rela tions, Sp atially Varying Properties , and Enhanced Budget and Velocity Output* (U.S. Geological Survey Techniques and Methods) [Unpublished report]. U.S Geological Survey.

Walvoord, M. A., & Kurylyk, B. L. (2016). Hydrologic Impacts of Thawing Permafrost—A Review. *Vadose Zone Journal*, *15*(6), vzj2016.01.0010. https://doi.org/10.2136/vzj2016.01.0010

Wang, C., Lai, Y., Yu, F., & Li, S. (2018). Estimating the freezing-thawing hysteresis of chloride saline soils based on the phase transition theory. *Applied Thermal Engineering*, *135*, 22–33. https://doi.org/10.1016/j.applthermaleng.2018.02.039

Wang, L., Zhou, J., Qi, J., Sun, L., Yang, K., Tian, L., Lin, Y., Liu, W., Shrestha, M., Xue, Y., Koike, T., Ma, Y., Li, X., Chen, Y., Chen, D., Piao, S., & Lu, H. (2017). Development of a land surface model with coupled snow and frozen soil physics. *Water Resources Research*, *53*(6), 5085–5103. https://doi.org/10.1002/2017WR020451

Watanabe, K., Kito, T., Wake, T., & Sakai, M. (2011). Freezing experiments on unsaturated sand, loam and silt loam. *Annals of Glaciology*, *52*(58), 37–43. https://doi.org/10.3189/172756411797252220

Watanabe, K., & Osada, Y. (2017). Simultaneous measurement of unfrozen water content and hydraulic conductivity of partially frozen soil near 0°C. *Cold Regions Science and Technology*, *142*, 79–84. https://doi.org/10.1016/j.coldregions.2017.08.002

Williams, P. J. (1964). Unfrozen Water Content of Frozen Soils and Soil Moisture Suction. *Géotechnique*, *14*(3), 231–246. https://doi.org/10.1680/geot.1964.14.3.231

Williams, P. J., & Smith, M. W. (1989). *The Frozen Earth: Fundamentals of Geocryology*. Cambridge University Press. https://doi.org/10.1017/CBO9780511564437

Yoshikawa, K., & Overduin, P. P. (2005). Comparing unfrozen water content measurements of frozen soil using recently developed commercial sensors. *Cold Regions Science and Technology*, *42*(3), 250–256. https://doi.org/10.1016/j.coldregions.2005.03.001

Zhang, L., Yang, C., Wang, D., Zhang, P., & Zhang, Y. (2022). Freezing point depression of soil water depending on its non-uniform nature in pore water pressure. *Geoderma*, *412*, 115724. https://doi.org/10.1016/j.geoderma.2022.115724

Zhang, S., Teng, J., He, Z., & Sheng, D. (2016). Importance of vapor flow in unsaturated freezing soil: A numerical study. *Cold Regions Science and Technology*, *126*. https://doi.org/10.1016/j.coldregions.2016.02.011

Zhang, X., Sun, S. F., & Xue, Y. (2007). Development and Testing of a Frozen Soil Parameterization for Cold Region Studies. *Journal of Hydrometeorology*, *8*(4), 690–701. https://doi.org/10.1175/JHM605.1

Zhao, L., Gray, D. M., & Male, D. H. (1997). Numerical analysis of simultaneous heat and mass transfer during infiltration into frozen ground. *Journal of Hydrology*, *200*(1), 345–363. https://doi.org/10.1016/S0022-1694(97)00028-0

Appendix

Figure A1 shows an example of the nonlinear least-squares optimization plots of 416 experimental soil datasets used to determine the *w* parameter values for the exponential freezing function. The soil dataset can be found in an open-sourced repository by (Devoie *et al*., 2022).

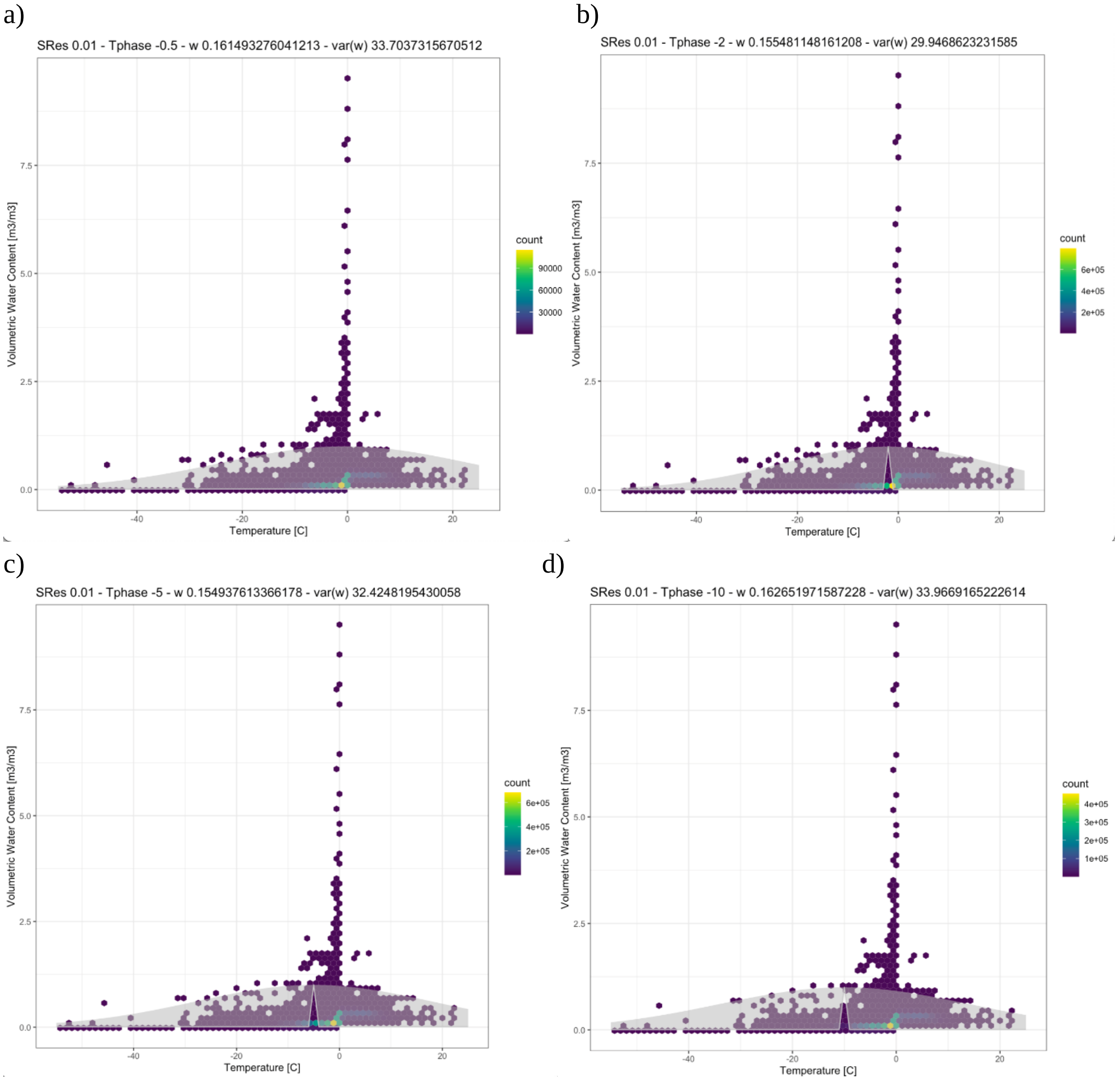

Figure A1. Plotted function used to fit w parameter to S_{WRES} = 0.01 with (a) T_{WRES} = –0.5° C, (b) T_{WRES} = –2 °C, (c) T_{WRES} = –5 °C and (d) T_{WRES} = –10 °C.

Figure A2 show the nonlinear least-squares optimization plots of 416 experimental soil datasets used to determine the α and β parameter values for the power law freezing function. The soil dataset can be found in an open-sourced repository by (Devoie *et al*., 2022).

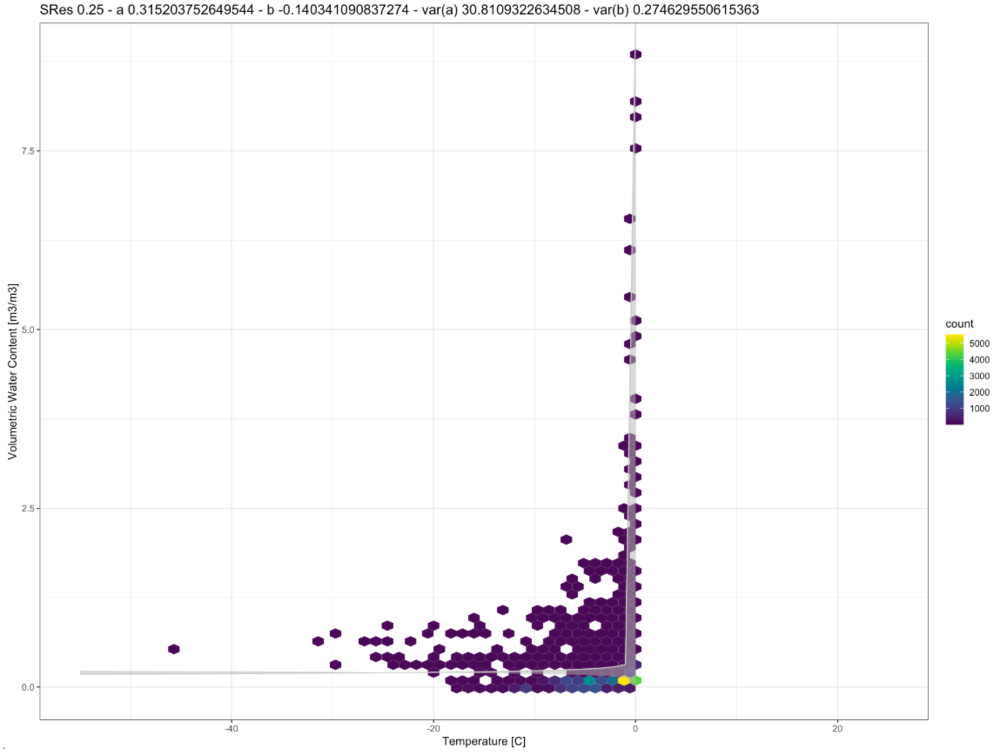

Figure A2. Plotted function used to fit α and β parameters to S_{WRES} = 0.25.